UNIVERSITY OF WARMIA AND MAZURY IN OLSZTYN

Technical Sciences

19(2) 2016

PUBLISHER UWM

OLSZTYN 2016

The Technical Sciences is indexed and abstracted in BazTech (http://baztech.icm.edu.pl) and in IC Journal Master List (http://journals.indexcopernicus.com)

The Journal is available in electronic form on the web sites
http://www.uwm.edu.pl/techsci (subpage Issues)
http://wydawnictwo.uwm.edu.pl (subpage Czytelnia)

The electronic edition is the primary version of the Journal

PL ISSN 1505-4675
e-ISNN 2083-4527

Address
ul. Jana Heweliusza 14
10-718 Olsztyn-Kortowo, Poland
tel.: +48 89 523 36 61
fax: +48 89 523 34 38
e-mail: wydawca@uwm.edu.pl

Ark. wyd. 7,08, ark. druk. 6,0, nakład 95 egz.
Druk – Zakład Poligraficzny UWM w Olsztynie
zam. nr 645

Contents

Biosystem Engineering

Geodesy and Cartography

Information Technology

Mechanical Engineering

Technical Sciences, 2016, 19(2) 103–115

Quarterly peer-reviewed scientific journal
ISSN 1505-4675
e-ISSN 2083-4527
TECHNICAL SCIENCES
Homepage: www.uwm.edu.pl/techsci/

BASIC PHYSICAL PROPERTIES OF NORWAY SPRUCE (*PICEA ABIES* (L.) KARST.) SEEDS

Zdzisław Kaliniewicz, Piotr Markowski, Andrzej Anders, Beata Jadwisieńczak, Tadeusz Rawa, Damian Szczechowicz

Department of Heavy Duty Machines and Research Methodology
University of Warmia and Mazury in Olsztyn

Received 21 November 2015, accepted 15 March 2016, available online 22 March 2016.

Key words: seeds, dimensions, seed mass, range of variations, correlation, separation.

Abstract

The range of variations in a given separation parameter and its relationships with other attributes have to be determined for designing seed cleaning and sorting processes. In this study, those relationships were determined for five batches of Norway spruce seeds supplied by a seed extraction plant in Jedwabno. The seeds were harvested from seed stands in northern Poland. The terminal velocity, length, width, thickness and mass of every seed were determined. The results were used to calculate the geometric mean diameter, aspect ratio, sphericity index and density of the evaluated seeds. Those parameters were compared by analysis of variance and linear correlation analysis. Similarities in the average values of all physical properties were noted only between seeds harvested in the same seed zone, from tree stands occupying the same habitat type. The analyzed seeds can be effectively separated into mass fractions with the use of traditional sorting devices such as pneumatic separators, mesh sieves with longitudinal or round openings, cylindrical graders, winnowing machines and pneumatic sieves, in order to achieve more uniform seedling emergence when each seed fraction is sown separately.

Symbols

D_g – geometric mean diameter of a seed, mm,
m – seed mass, mg,
R – aspect ratio, %,
SD – standard deviation of trait,
T, W, L – seed thickness, width and length, mm,
v – terminal velocity, m s^{-1},
x – average value of trait,
ρ – seed density, g cm^{-3},
Φ – sphericity index, %.

Correspondence: Zdzisław Kaliniewicz, Katedra Maszyn Roboczych i Metodologii Badań, Uniwersytet Warmińsko-Mazurski, ul. Oczapowskiego 11/B112, 10-719 Olsztyn, phone: +48 89 523 39 34, e-mail: zdzislaw.kaliniewicz@uwm.edu.pl

Introduction

The Norway spruce (*Picea abies* (L.) Karst.) is a tree that grows up to 50 m in height and 200 cm in diameter at breast height. Its geographic range covers mostly Central and Northern Europe where it adapts to various climate conditions. The Norway spruce requires a growing season of at least 60 days and a winter dormancy period of minimum 120 days with sub-zero temperatures. In optimal habitats, the Norway spruce is a shade-tolerant species, but it thrives under direct exposure to sunlight. The species has moderate soil requirements, but has a preference for soils with a relatively high moisture content. The Norway spruce thrives on fresh brown soils developed from sandy loam, characterized by a moderate nutrient content, relatively low acidity and a relatively low water table (MURAT 2002, JAWORSKI 2011).

The Norway spruce grows slowly in the first years of life, and its growth is accelerated at 30 to 50 years of age. Its growth rate decreases in old age, but the species continues to grow until the end of its life cycle (MURAT 2002, JAWORSKI 2011). The Norway spruce begins to produce seeds at 20–30 years of age in open spaces and at around 60 years of age in dense stands (*Nasiennictwo leśnych drzew*... 1995, MURAT 2002). Cones harvested at the turn of November and December are husked, and the extracted seeds are dewinged. Spruce seeds have a uniform dark reddish-brown color (Fig. 1), they reach 4–5 mm in length, they are rounded at one end and tapered to a point at the other end (*Nasiennictwo leśnych drzew*... 1995). Spruce seeds provide food for birds and small forest animals, including woodpeckers, squirrels and pygmy shrews (MURAT 2002).

Norway spruce seeds can be effectively preserved by drying. They are stored in air-tight containers at a temperature of 2–5°C, and their moisture content is reduced to approximately 6–7%. They can be stored in the above conditions for up to 6 years without significant loss of germination capacity. Seed vigor can be maintained for even 30 years by further reducing moisture content and storing seeds at sub-zero temperatures (MURAT 2002, ANIŚKO et al. 2006).

According to the literature (MIKOLA 1980, KHAN 2004, PARKER et al. 2006, SHANKAR 2006, UPADHAYA et al. 2007, WU, DU 2007, CASTRO et al. 2008, NORDEN et al. 2009, BURACZYK 2010, KALINIEWICZ 2012a), seed mass is one of the key determinants of germination and seedling growth. Plumper seeds generally germinate better due to a higher content of nutrient reserves which are required for seedling emergence. Depending on the species, germination rate can be proportional or inversely proportional to seed mass. The separation of seeds into mass fractions promotes uniform germination, which is a very important consideration in tree nurseries. However, seeds are difficult to sort

Fig. 1. Norway spruce seeds

based on mass as a separation parameter. For this reason, further research is needed to identify the relationships between the physical properties of seeds and use them to design seed separation process, in particular those that involve traditional sorting devices (pneumatic separators and mesh sieves).

The objective of this study was to determine the variations in and the correlations between the terminal velocity, basic dimensions (length, width and thickness), mass and density of Norway spruce seeds to select optimal parameters for seed separation processes.

Materials and Methods

The experimental material comprised five batches of Norway spruce seeds supplied by a seed extraction plant in Jedwabno in 2012. Three batches constituted seed propagation material from an identified source, and two batches contained selected and certified seeds. The seeds were extracted from cones harvested in three seed zones in northern Poland (Fig. 2). The analyzed batches were harvested from the following tree stands:

a) registration No. MP/1/46879/06, category of seed propagation material – from an identified source, type – tree stand, region of provenance – 205, municipality – Purda, geographic location – 53.39°N, 20.41°E, forest habitat – fresh mixed coniferous forest, age – 86 years (symbol: IS-1),

b) registration No. MP/1/46252/06, category of seed propagation material (deleted) – from an identified source, type – tree stand, region of provenance – 205, municipality – Szczytno, geographic location 53.33-53.40°N, 20.49-21.03°E, forest habitat – fresh mixed coniferous forest, age – 107 years (symbol: IS-2),

c) registration No. MP/1/45601/06, category of seed propagation material (deleted) – from an identified source, type – tree stand, region of provenance – 205, municipality – Szczytno, geographic location 53.29°N, 21.06°E, forest habitat – moist mixed coniferous forest, age – 131 years (symbol: IS-3),

d) registration No. MP/2/31324/05, category of seed propagation material (deleted) – selected seeds, type – tree stand, region of provenance – 451, municipality – Płośnica, geographic location 53.14°N, 20.04°E, forest habitat – fresh mixed forest, age – 113 years (symbol: SS),

e) registration No. MP/3/41105/05, category of seed propagation material – certified seeds, type – plantation, region of provenance – 103, municipality – Braniewo, geographic location 54.24°N, 19.50°E, forest habitat – moist mixed forest, age – 22 years (symbol: CS).

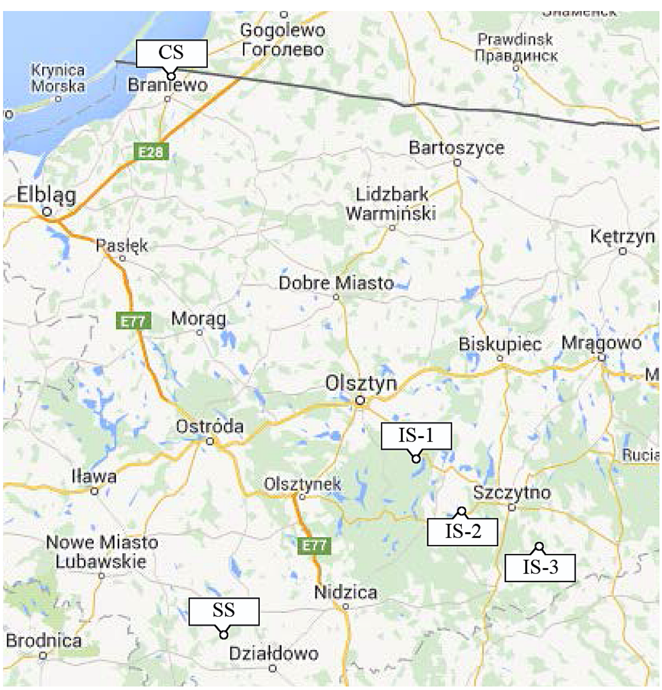

Fig. 2. Geographic location of Norway spruce stands

Analytical samples from every batch of seeds were collected by halving (*Nasiennictwo leśnych drzew...* 1995). Initial samples of approximately 0.5 kg were halved, and one half was randomly selected for successive halving. The above procedure was repeated to produce samples of around 100 seeds each. The ultimate sample size ranged from 85 (IS-3) to 116 (IS-2) seeds. The remaining seeds were sampled to determine their moisture content in the Radwag MAX 50/WH drying oven with a weighing scale (Radwag Radom, Poland). The analyzed seeds were characterized by a similar moisture content in the range of 6.8% to 7.3%.

In the first stage of the study, terminal velocity was determined in the Petkus K-293 pneumatic classifier (Petkus Technologie GmbH, Germany) with the resolution of 0.11 m s^{-1} (air flow rate – 1 m^3 h^{-1}). To facilitate the measurements, seeds were divided into fractions, and air stream velocity was changed every 0.55 m s^{-1}, which produced 7 to 9 fractions for every seed batch. Air stream velocity was adjusted within the range of variations corresponding to a given fraction, at 0.11 m s^{-1} intervals, and seeds were fed into the classifier. Seeds that fell to the bottom were fed back into the classifier and air stream speed was increased. The terminal velocity of a given seed was determined as the arithmetic mean of two air stream speeds calculated based on two consecutive measurements: the speed at which a seed fell to the bottom in the air stream and the speed at which a seed was lifted by the air stream.

The length and width of seeds were measured to the nearest 0.02 mm. Every seed was placed on a transparent slide and analyzed in the MWM 2325 workshop microscope (PZO Warszawa, Poland). The micrometric gauge was adjusted to move the stage to a position where the line on the eyepiece coincided with the contour of the beginning of the seed. The position was read from the gauge. The stage was then moved to a position where the line on the eyepiece coincided with the contour of the end of the seed, and the result was red from the gauge. The measured parameter was the difference between the first and the last reading. Seed width was measured with the use of the second micrometric gauge in an identical procedure. Seed thickness was determined with a dial thickness gauge to the nearest 0.01 mm. The thickness gauge was reset, the sensor plate was lifted, and individual seeds were placed inside the device, always on the same wall. The sensor plate was lowered and seed thickness was read from the dial.

Seed mass was determined on the WAA 100/C/2 weighing scale with 0.1 mg resolution (Radwag Radom, Poland).

In the second stage of the study, the measurements were used to determine:

a) geometric mean diameter D_g, aspect ratio R and sphericity index Φ (MOHSENIN 1986):

$$R = \frac{W}{L} \cdot 100 \tag{2}$$

$$\Phi = \frac{(T \cdot W \cdot L)^{\frac{1}{3}}}{L} \cdot 100 \tag{3}$$

b) seed density ρ – based on the volumetric coefficient of proportionality determined experimentally by KALINIEWICZ et al. (2012b) with a liquid pycnometer:

$$\rho = \frac{m}{0.522 \cdot T \cdot W \cdot L} \tag{4}$$

Based on their mass, seeds were divided into three size categories: small seeds ($m < x–SD$), medium-sized seeds (x–SD ≤ m ≤ x+SD) and large seeds (m > x+SD). The results were rounded off to the next multiple of 1.

The results were processed in the Statistica v. 12.5 application with the use of popular statistical procedures such as one-way ANOVA and linear correlation analysis (RABIEJ 2012). The calculations were performed at a significance level of 0.05.

Results and Discussion

Based on the number of seeds in each sample and the standard deviations of the analyzed physical properties of Norway spruce seeds, the errors in the mean values of the evaluated properties did not exceed:
- for the terminal velocity – 0.2 m s^{-1},
- for the seed thickness – 0.04 mm,
- for the seed width – 0.07 mm,
- for the seed length – 0.1 mm,
- for the seed mass – 0.4 mg.

The physical properties of seeds are presented in Table 1. Statistically significant differences in the values of all analyzed properties and parameters were not noted only between seed batches IS-1 and IS-2. This could result from the fact that seeds of those batches were harvested from tree stands located in the same seed zone (with identical climatic and geomorphological conditions), occupying the same habitat type (fresh mixed coniferous forest). In the remaining cases, significant differences between the properties of the analyzed seeds were noted locally. This could be due to differences in habitat and soil type which, according to numerous authors (KLUCZYŃSKI 1992, *Nasiennictwo* *leśnych drzew...* 1995, KARLSSON, ÖRLANDER 2002, SIVACIOĞLU 2010), can considerably influence seed size. Seed size can also be determined by the age of the tree stand. KALINIEWICZ et al. (2013) demonstrated that the dimensions and mass of Scots pine seeds decreased with tree age. The largest number of the highest average values of the analyzed seed parameters was noted in seed batch IS-1 (terminal velocity, seed thickness, seed width, geometric mean diameter, aspect ratio and sphericity index), and the smallest number – in batch CS (seed thickness, seed width, seed length, geometric mean diameter). Seed density was the only parameter that was higher in batch CS, which indicates that those seeds were characterized by higher proportions of primary endosperm and germ than seeds from the other batches.

Table 1

Range of variations in the physical properties of Norway spruce seeds, with an indication of significant differences

Physical property/ indicator	Seed batch (sample size)				
	IS-1 (113) x±SD	IS-2 (116) x±SD	IS-3 (85) x±SD	SS (112) x±SD	CS (114) x±SD
v [m s^{-1}]	7.92±0.75^{a}	7.88±0.80^{a}	7.49±0.74^{b}	7.45±0.63^{b}	7.61±0.79^{b}
T [mm]	1.53±0.15^{a}	1.52±0.16^{a}	1.46±0.15^{b}	1.46±0.16^{b}	1.44±0.15^{b}
W [mm]	2.25±0.26^{a}	2.23±0.29^{a}	2.05±0.26^{bc}	2.12±0.31^{b}	2.04±0.25^{c}
L [mm]	4.15±0.44^{a}	4.22±0.45^{a}	4.15±0.43^{a}	4.11±0.44^{ab}	4.00±0.41^{b}
m [mg]	6.82±1.77^{a}	6.84±1.80^{a}	6.12±1.40^{b}	6.10±1.55^{b}	6.16±1.47^{b}
D_g [mm]	2.42±0.20^{a}	2.42±0.22^{a}	2.31±0.16^{bc}	2.33±0.23^{b}	2.27±0.17^{c}
R [%]	54.69±7.52^{a}	53.20±7.26^{ab}	50.10±8.51^{c}	51.91±7.01^{bc}	51.23±7.97^{bc}
Φ [%]	58.65±4.11^{a}	57.65±4.11^{ab}	55.97±5.05^{c}	56.93±4.16^{bc}	56.98±4.96^{bc}
ρ [g cm^{-3}]	0.91±0.11^{c}	0.91±0.12^{c}	0.95±0.18^{b}	0.91±0.14^{c}	1.01±0.17^{a}

$^{a, b, c}$ – different letters indicate statistically significant differences in the value of a given parameter (indicator).

The average terminal velocity was determined in the range of 7.45 to 7.92 m s^{-1}, and it was similar to that noted by KALINIEWICZ et al. (2012a), but approximately 20% higher than that reported by TYLEK (1999) in a study of seeds from southern Poland. Seeds harvested in southern Poland are larger and heavier (*Nasiennictwo leśnych drzew...* 1995) than those growing in the northern parts of the country. The above observations were confirmed by SZCZYGIEŁ (1981), CZERNIK (1983), TYLEK (1998) and OLEKSYN et al. (1998). Those results indicate that seed dimensions and seed mass decrease with an increase in the northern latitude of tree stands (MIKOLA 1980, OLEKSYN et al. 2001). Norway spruce seeds resemble Jack pine seeds in width, and shore pine and red pine seeds in length (CARRILLO-GAVILÁN et al. 2010). The analyzed seeds are similar to fenugreek seeds in thickness (ALTUNTAŞ et al. 2005) and to flaxseed in geometric mean diameter (PRADHAN et al. 2010). The aspect ratio of Norway spruce seeds was estimated at 52%, and it was only 4% lower than that reported by Tylek (1998) despite significant differences in the dimensions of the compared seeds. The analyzed seeds were similar to wheat grain in terms of their aspect ratio and sphericity index (Hebda, Micek 2005, Frączek, Wróbel 2006, Kalkan, Kara 2011, Markowski et al. 2013).

A linear correlation analysis of selected physical properties of Norway spruce seeds (Table 2) revealed that most of them (excluding 18 cases) were strongly correlated at a significance level of 0.05. Practical significance, where the correlation coefficient was minimum 0.4, was noted in 43 out of 90 cases.

Table 2

Coefficients of linear correlation between selected physical properties of Norway spruce seeds

Seed batch	Physical property	*T*	*W*	*L*	*m*	*ρ*
IS-1	*v*	**0.421**	**0.314**	**0.324**	**0.569**	**0.302**
	T	1	**0.463**	**0.536**	**0.683**	**-0.247**
	W		1	**0.250**	**0.652**	**-0.214**
	L			1	**0.704**	-0.096
	m				1	**0.245**
IS-2	*v*	**0.522**	**0.306**	**0.273**	**0.639**	**0.328**
	T	1	**0.392**	**0.441**	**0.680**	-0.161
	W		1	**0.390**	**0.645**	**-0.299**
	L			1	**0.706**	-0.158
	m				1	**0.215**
IS-3	*v*	**0.528**	0.177	0.140	**0.743**	**0.421**
	T	1	0.199	0.115	**0.558**	-0.022
	W		1	-0.062	**0.285**	**-0.376**
	L			1	**0.376**	-0.198
	m				1	**0.487**
SS	*v*	**0.508**	**0.504**	**0.400**	**0.633**	-0.008
	T	1	**0.512**	**0.460**	**0.699**	**-0.326**
	W		1	**0.472**	**0.699**	**-0.470**
	L			1	**0.768**	-0.179
	m				1	0.029
CS	*v*	**0.511**	**0.249**	0.138	**0.736**	**0.514**
	T	1	**0.422**	0.164	**0.566**	-0.152
	W		1	0.155	**0.496**	**-0.296**
	L			1	**0.510**	-0.063
	m				1	**0.445**
Total	*v*	**0.518**	**0.352**	**0.265**	**0.675**	**0.279**
	T	1	**0.451**	**0.376**	**0.661**	**-0.212**
	W		1	**0.294**	**0.602**	**-0.371**
	L			1	**0.635**	**-0.164**
	m				1	**0.227**

Values in bold represent statistically significant correlations.

The highest value of the correlation coefficient (0.768) was observed between the length and mass of seeds in batch SS, and the lowest (0.022) – between the thickness and density of seeds in batch IS-3. The following seed parameters were most highly correlated with seed mass in each batch:

– terminal velocity (batches IS-3 and CS),
– thickness and width (batch SS),
– length (batches IS-1 and IS-2).

In view of the fact that the effects of the terminal velocity and basic dimensions of seeds on their mass are similar, it can be assumed that Norway spruce seeds can be separated into mass fractions with the use of traditional cleaning and sorting devices (pneumatic separators, separator buckets, graders and complex machines comprising separating elements).

In our study, the average mass of Norway spruce seeds was determined at 6.42±1.65 mg. The classification boundaries were rounded off, and seeds were divided into three size fractions: small seeds (m<5 mg), medium-sized seeds (m=5–8 mg) and large seeds (m>8 mg). The analyzed material contained 16.3% of small seeds, 70.2% of medium-sized seeds and 13.5% of large seeds. The distribution of terminal velocity, seed thickness, width and length values across size fractions is presented in Figure 3. The present results indicate that all four parameters can be used to sort Norway spruce seeds into fractions because they ensure maximum mass uniformity.

When air stream speed in two tunnels is set to 6.6 m s^{-1} and 8.8 m s^{-1}, seeds will be separated into three fractions, where the lightest fraction will comprise around 37% of small seeds and only 3% of medium-sized seeds, and the heaviest fraction will contain approximately 25% of large seeds and 2% of medium-sized seeds. TYLEK (1999) also observed that Norway spruce seeds can be effectively sorted with the use of pneumatic separators where viable (full) seeds are separated from non-viable (empty) seeds in a stream of air.

Mesh sieves with ≠1.4 mm and ≠1.6 mm longitudinal openings are recommended for sorting seeds based on their thickness. The sifted fraction will contain around 71% of small seeds and 26% of medium-sized seeds, and the retained fraction will be composed of around 6% small seeds, 15% of medium-sized seeds and 62% large seeds. Each fraction will have the following composition:

– fine-sized fraction (T≤1.4 mm) – 39% of small seeds and 61% of medium-sized seeds,

– medium-sized fraction (T=1.4-1.6 mm) – 7.6% of small seeds, 82.2% of medium-sized seeds and 10.2% of large seeds,

– coarse-sized fraction (T>1.6 mm) – 4.7% of small seeds, 52.8% of medium-sized seeds and 42.5% of large seeds.

Mesh sieves with ø2.0 mm and ø2.5 mm round openings are recommended for sorting seeds based on their width. The sifted fraction will contain approximately 69% of small seeds, 30% of medium-sized seeds and 1% of large seeds, and the retained fraction will be composed of around 1% of small seeds, 7% of medium-sized seeds and 48% of large seeds.

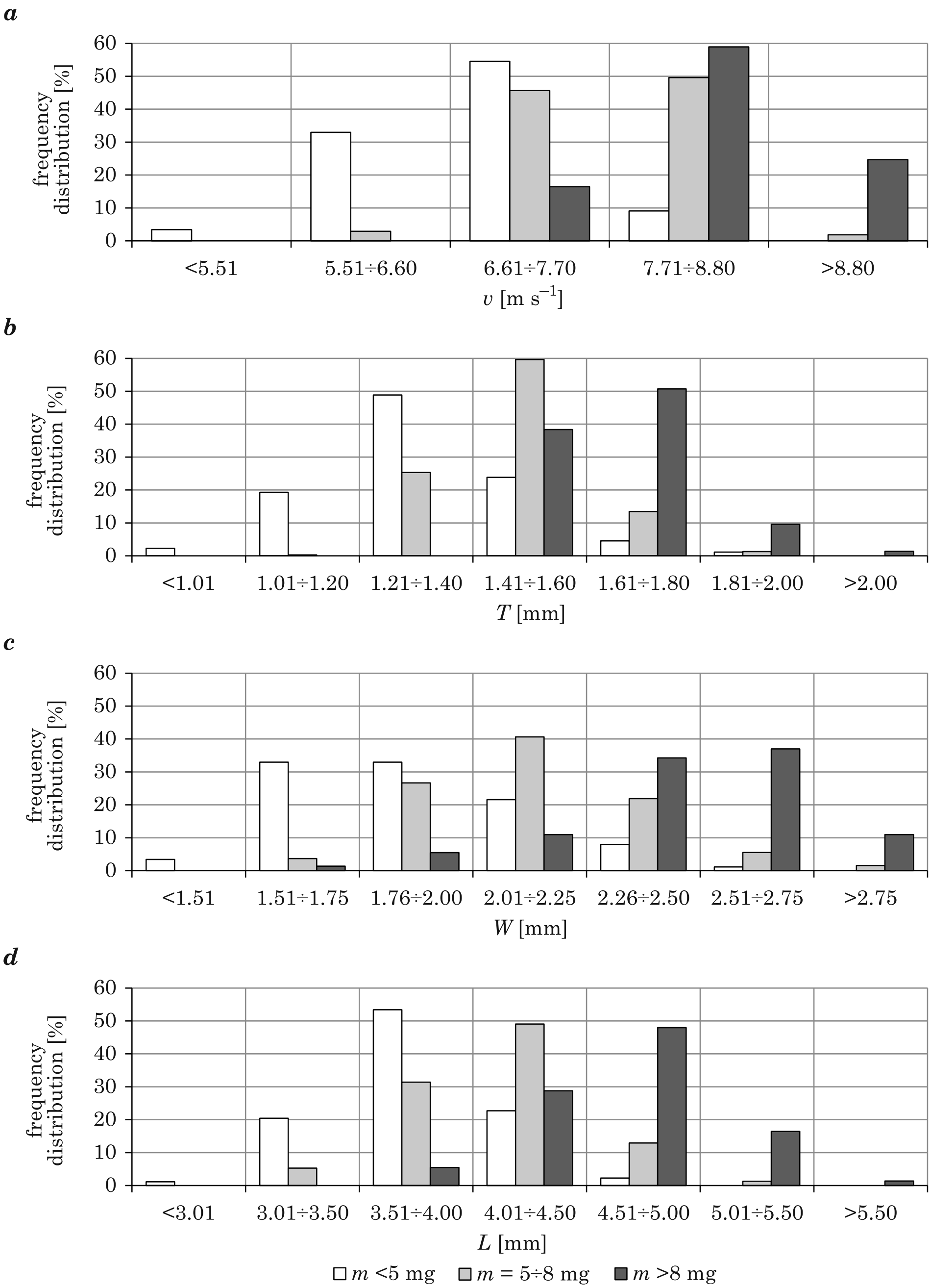

Fig. 3. Distribution of the terminal velocity (*a*), thickness (*b*), width (*c*) and length (*d*) of seeds in three mass fractions

When sorting seeds based on their length, two cylindrical graders with ø4.0 mm and ø4.5 mm indentations should be used. The fraction in the smaller trough will contain approximately 75% of small seeds, 37% of medium-sized seeds and 5.5% large seeds, whereas the fraction of the longest seeds (which are not carried to the trough in the grader with larger indentations) – around 2% of small seeds, 14% of medium-sized seeds and 65% of large seeds.

The results of the analysis (Table 3) indicate that the fractioning process classifies seeds into groups of similar size. The coefficient of variation of seed mass was determined at 26% before separation, and it was reduced in the resulting fractions. For example, in the medium-sized fraction, the above parameter was decreased by 20÷27% in comparison with unsorted seeds.

Table 3

Coefficient of variation (%) of seed mass in three seed fractions

Separation parameter	Seed fraction	Coefficient of variation of seed mass	
		fraction	total
v	I (v<6.6 m s^{-1})	24.21	25.67
	II (v=6.6÷8.8 m s^{-1})	20.56	
	III (v>8.8 m s^{-1})	20.94	
T	I (T<1.4 mm)	23.10	
	II (T=1.4÷1.6 mm)	19.12	
	III (T>1.6 mm)	22.31	
W	I (W<2.0 mm)	25.34	
	II (W=2.0÷2.5 mm)	18.78	
	III (W>2.5 mm)	23.68	
L	I (L<4.0 mm)	23.33	
	II (L=4.0÷4.5 mm)	18.75	
	III (L>4.5 mm)	22.05	

Conclusions

1. The results of this study confirmed the well-known fact the physical parameters of seeds, including Norway spruce seeds, are determined, among other factors, by habitat type and the geographical location of a seed stand. The average values of all physical properties of seeds from the analyzed batched did not differ significantly only in seeds harvested in the same seed zone, from tree stands occupying the same habitat type.

2. A linear correlation analysis revealed the strongest relationships between seed mass and terminal velocity or one of the basic seed dimensions (thickness, width, length). The degree of correlation was related to the specific characteristics of seeds in a given batch, but the values of correlation coefficients were generally similar. This indicates that Norway spruce seeds can be

effectively separated with the use of traditional cleaning and sorting machines and devices.

3. When Norway spruce seeds are sorted with a pneumatic separator, two speeds of the air stream should be set, i.e. around 6.6 m s^{-1} and 8.8 m s^{-1}. The separation process can also be performed using two mesh sieves with ≠1.4 mm and ≠1.6 mm longitudinal openings or two mesh sieves with ø2.0 mm and ø2.5 mm round openings. Another option is to use two cylindrical graders with ø4.0 mm and ø4.5 mm indentations. In each case, seeds will be separated into uniform mass fractions, thus improving seedling emergence uniformity.

References

ALTUNTAŞ E., ÖZGÖZ E., TAŞER Ö.F. 2005. *Some physical properties of fenugreek (Trigonella foenum-graceum L.) seeds*. Journal of Food Engineering, 71: 37–43.

ANIŚKO E., WITOWSKA O., ZAŁĘSKI A. 2006. *Effect of dryings conditions on viability of common birch, black alder, Scots pine and Norway spruce seeds*. Leśne Prace Badawcze, 2: 91–13.

BURACZYK W. 2010. *Seed characteristics and morphological features of Scots pine (Pinus sylvestris L.) seedlings*. Leśne Prace Badawcze, 71(1): 13–20.

CARRILLO-GAVILÁN M.A., LALAGÜE H., VILÀ M. 2010. *Comparing seed removal of 16 pine species differing in invasiveness*. Biological Invasions, 12: 2233–2242.

CASTRO J., REICH P.B., SÁNCHEZ-MIRANDA Á., GUERRERO J.D. 2008. *Evidence that the negative relationship between seed mass and relative growth rate is not physiological but linked to species identity: a within-family analysis of Scots pine*. Tree Physiology, 28: 1077–1082.

CZERNIK Z. 1983. *Studies of geometrical features of seeds of Scots pine, Norway spruce and European larch*. Sylwan, 7: 31–40.

FRĄCZEK J., WRÓBEL M. 2006. *Methodic aspects of seed shape assessment*. Inżynieria Rolnicza, 12: 155–163 (in Polish).

HEBDA T., MICEK P. 2005. *Dependences between geometrical features of cereal grain*. Inżynieria Rolnicza, 6: 233–241.

JAWORSKI A. 2011. *Hodowla lasu*. Tom III. *Charakterystyka hodowlana drzew i krzewów leśnych*. PWRiL, Warszawa.

KALINIEWICZ Z., MARKOWSKI P., RAWA T., GRABOWSKI A., FURA S. 2012a. *A correlation between germination capacity and selected physical characteristics of Norway spruce (Picea abies) seeds.* Inżynieria Przetwórstwa Spożywczego, 1/4: 13–17.

KALINIEWICZ Z., RAWA T., TYLEK P., MARKOWSKI P., ANDERS A., FURA S. 2013. *The effect of the age of Scots pine (Pinus sylvestris L.) stands on the physical properties of seeds and the operating parameters of cleaning machines*. Technical Sciences, 16(1): 63–72.

KALINIEWICZ Z., TYLEK P., MARKOWSKI P., ANDERS A., RAWA T., ZADROŻNY M. 2012b. *Determination of shape factors and volume coefficients of seeds from selected coniferous trees.* Technical Sciences, 15(2): 217–228.

KALKAN F., KARA M. 2011. *Handling, frictional and technological properties of wheat as affected by moisture content and cultivar*. Powder Technology, 213: 116–122.

KARLSSON CH., ÖRLANDER G. 2002. *Mineral nutrients in needles of Pinus sylvestris seed trees after relase cutting and their correlations with cone production and seed weight*. Forest Ecology and Management, 166: 183–191.

KHAN M.L. 2004. *Effects of seed mass on seedling success in Artocarpus heterophyllus L., a tropical tree species of north-east India*. Acta Oecologica, 25: 103–110.

KLUCZYŃSKI B. 1992. *Yielding and quality of Norway spruce [Picea abies (L.) Karst] seeds in dependence on the part of crown and chosen biological and site-related characteristics of trees*. Sylwan, 5: 25–35.

MARKOWSKI M., ŻUK-GOŁASZEWSKA K., KWIATKOWSKI D. 2013. *Influence of variety on selected physical and mechanical properties of wheat*. Industrial Crops Products, 47: 113–117.

MIKOLA J. 1980. *The effect of seed size and duration of growth on the height of Scots pine (Pinus sylvestris L.) and Norway spruce (Picea abies (L.) Karst.) provenances and progenies at the nursery stage*. Silva Fennica, 14(1): 84–94.

MOHSENIN N.N. 1986. *Physical properties of plant and animal materials*. Gordon and Breach Science Public, New York.

MURAT E. 2002. *Szczegółowa hodowla lasu*. Oficyna Edytorska „Wydawnictwo Świat", Warszawa.

Nasiennictwo leśnych drzew i krzewów iglastych. 1995. Ed. A. Załęski. Oficyna Edytorska „Wydawnictwo Świat", Warszawa.

NORDEN N., DAWS M.I., ANTOINE C., GONZALEZ M.A., GARWOOD N.C., CHAVE J. 2009. *The relationship between seed mass and mean time to germination for 1037 tree species across five tropical forests*. Functional Ecology, 23(1): 203–210.

OLEKSYN J., MODRZYŃSKI J., TJOELKER M.G., ŻYTKOWIAK R., REICH P.B., KAROLEWSKI P. 1998. *Growth and physiology of Picea abies populations from elevational transects: common garden evidence for altitudinal ecotypes and cold adaptation*. Functional Ecology, 12: 573–590.

OLEKSYN J., REICH P.B., TJOELKER M.G., CHALUPKA W. 2001. *Biogeographic differences in shoot elongation pattern among European Scots pine populations*. Forest Ecology and Management, 148: 207–220.

PARKER W.C., NOLAND T.L., MORNEAULT A.E. 2006. *The effects of seed mass on germination, seedling emergence, and early seedling growth of eastern white pine (Pinus strobus L.)*. New Forests, 32: 33–49.

PRADHAN R.C., MEDA V., NAIK S.N., TABIL L. 2010. *Physical properties of Canadian grown flaxseed in relation to its processing*. International Journal of Food Properties, 13: 732–743.

RABIEJ M. 2012. *Statystyka z programem Statistica*. Helion, Gliwice.

SHANKAR U. 2006. *Seed size as a predictor of germination success and early seedling growth in 'hollong' (Dipterocarpus macrocarpus Vesque)*. New Forests, 31: 305–320.

SIVACIOĞLU A. 2010. *Genetic variation in seed cone characteristics in a clonal seed orchard of Scots pine (Pinus sylvestris L.) grown in Kastamonu-Turkey*. Romanian Biotechnological Letters, 15(6): 5695–5701.

SZCZYGIEŁ K. 1981. *The effect of spruce seed weight upon the height of seedlings grown under optima conditions*. Sylwan, 1: 33–39.

TYLEK P. 1998. *Cechy planimetryczne nasion drzew liściastych*. Przegląd Techniki Rolniczej i Leśnej, 1: 22–24.

TYLEK P. 1999. *Problems of pneumatic selection of forest tree seeds*. Sylwan, 12: 65-72.

UPADHAYA K., PANDEY H.N., LAW P.S. 2007. *The effect of seed mass on germination, seedling survival and growth in Prunus jenkinsii Hook.f. & Thoms*. Turkish Journal of Botany, 31: 31–36.

WU G., DU G. 2007. *Germination is related to seed mass in grasses (Poaceae) of the eastern Qinghai-Tibetan Plateau, China*. Nordic Journal of Botany, 25(5–6): 361–365.

Technical Sciences, 2016, 19(2) 117–127

UNIWERSYTET WARMIŃSKO-MAZURSKI W OLSZTYNIE

Quarterly peer-reviewed scientific journal
ISSN 1505-4675
e-ISSN 2083-4527
TECHNICAL SCIENCES
Homepage: www.uwm.edu.pl/techsci/

INFLUENCE OF HUMAN BODY ON RADIO SIGNAL STRENGTH INDICATOR READINGS IN INDOOR POSITIONING SYSTEMS

***Jacek Rapiński*[1], *Daniel Zinkiewicz*[2], *Tomasz Stanislawek*[2]**

[1] The Faculty of Geodesy, Geospatial and Civil Engineering,
University of Warmia and Mazury in Olsztyn
[2] WASAT sp. z o.o., Warszawa

Received 7 December 2015, accepted 23 March 2016, available online 6 May 2016.

Key words: Radio Signal Strength Indicator, fingerprint, indoor positioning.

Abstract

In this paper the basic assumptions of a Radio Signal Strength Indicator – based fingerprint and the influence of human body on the results are presented. The main focus is put on the influence of the obstruction of line-of-sight between access point and transceiver by a human body. This issue must be corrected in order to gain more accurate and reliable results of the positioning. The mathematical model for correction of this issue is proposed along with some examples. The examples are based on the real measurements made by authors. Presented correction formula allows to minimize the influence of the user – access point direction on the results obtained during fingerprint creation and positioning.

Introduction

The positioning systems based on a Radio Signal Strength Indicator (RSSI) are widely described and had been investigated by many authors (GANSEMER 2010, SHEN et al. 2005, KUO et al. 2010). They can operate using one of available wireless communication systems like WiFi, Bluetooth, ZigBee or XBee. There is a lot of phenomena connected with electromagnetic wave propagation, that can cause the RSSI reading to vary. One of them is the

Correspondence: Jacek Rapiński, Instytut Geodezji, Uniwersytet Warmińsko-Mazurski, ul. Oczapowskiego 2, 10-719 Olsztyn, phone: 89 523 42 04, e-mail: jrap3@wp.pl

attenuation and diffraction of the signal caused by a human body. When a person is holding a hand-held transceiver the direction to the access point (AP) can be obstructed by his body (Fig. 1). This will have a significant influence on the RSSI reading.

The radio signal is propagated according to the Friis equation (FRIIS 1946), which can be presented in its simplest form as:

$$\frac{P_r}{P_t} = G_r G_t \left(\frac{\lambda}{4\pi R}\right)^2 \tag{1}$$

where:
P_r – received signal strength,
P_t – transmitted signal strength,
G_t – transmitter antenna gain,
G_r – receiver antenna gain,
λ – wavelength,
R – receiver – transmitter distance.

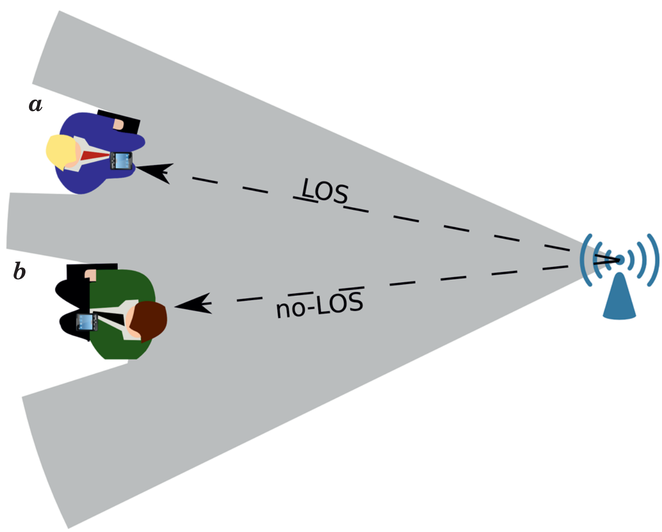

Fig. 1. Human body obstructing the LOS propagation: a – has line of sight, b – is obstructed by the users body

This equation is only true in theoretical ideal conditions. It assumes that a) the wavelength λ is much smaller than the distance R, b) the antennas are unobstructed and there is no multipath present, c) there is no impedance mismatch, no misalignment of polarization and no signal loss on the cables between transceivers and antennas. Because of this simplifications the equation cannot be directly used for distance calculation and range-based positioning (like trilateration). This is the reason for which the fingerprint methods were invented. In this methods the distance to the AP is not calculated and the positioning is based on matching the users observations with preliminary prepared maps of RSSI.

RSSI mapping

The RSSI parameter is defined in IEEE Standards Association (2012) and its characterization and description is available for example in BARDWELL (2004). The original use of this parameter was to establish a threshold for the wireless communication rather than positioning. This parameter has its limitations which results from its origins and compact size of communication devices. The most important issue is that the RSSI is not defined in a strict way. The IEEE Standards Association (2012) defines this parameter as a value between 0 and $RSSI_{max}$, where nothing is said about the value of $RSSI_{max}$. Therefore the upper limit of the RSSI value depends on the manufacturer of the transceiver. The resolution of the reading is device-dependent and affect the positioning accuracy. The dependency between IEEE 802.11 RSSI value and signal strength in dBm for various integrated circuit manufacturers is presented in Figure 2.

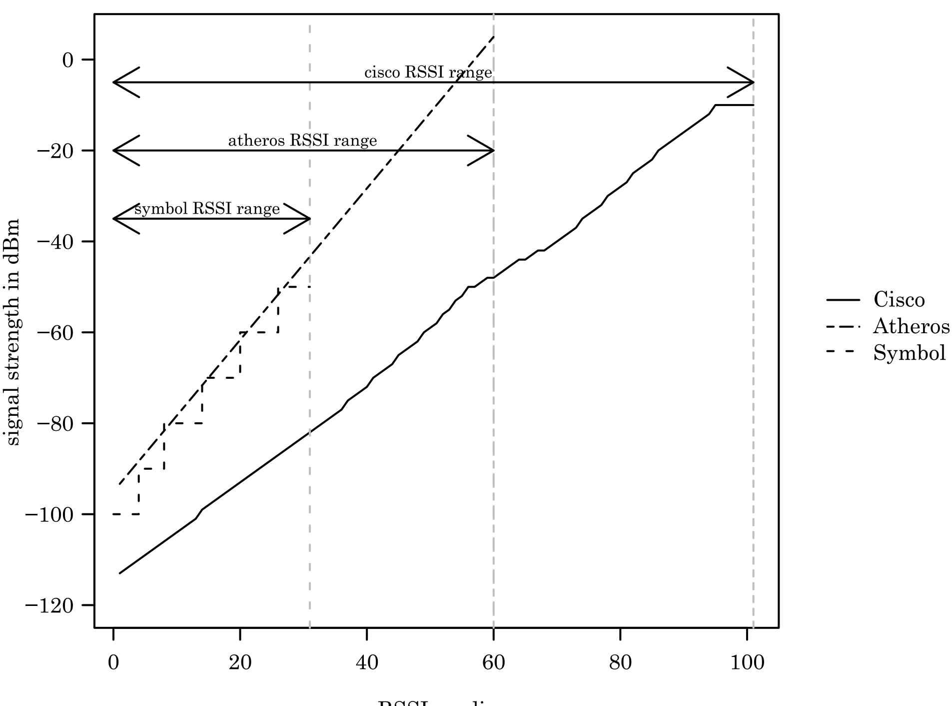

Fig. 2. Dependency between IEEE 802.11 RSSI value and signal strength in dBm for various integrated circuit manufacturers

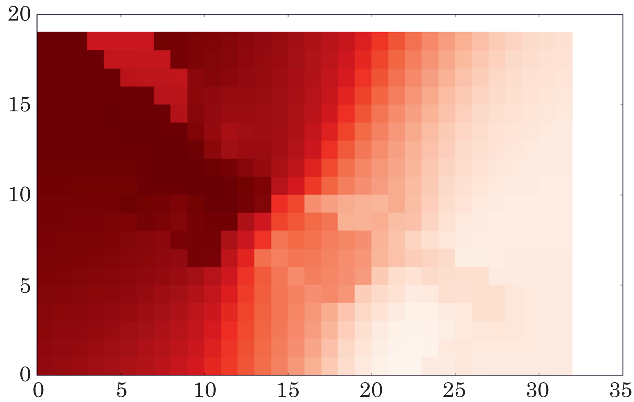

Fig. 3. Example of a heatmap for a single AP (dark = strong signal, light = light signal)

In the fingerprint method mapping of the RSSI of a considered area is required. The idea is to obtain a spatially distributed map of RSSI readings. The pre-surveyed values of the signal strength can be represented as a heat-map. The collection of the data for a heat map must be performed in a uniform way using the same device. Two ways of achieving the data are possible – by sampling the RSSI values in a uniform grid or by sampling in non uniform way and interpolating. Another option is to use the irregular heat map (points with corresponding RSSI values) as a nodes to which the positioning algorithm will try to „snap" the users location. The example of a heat map for a single AP is presented in Figure 3, where darker color represents stronger signal.

Positioning

The RSSI maps are created for each visible AP. The vector of signal strength values collected during localization is compared to these maps. User position is assumed in the place where the probed values are most closest (or most similar) to RSSI maps. This is illustrated in Figure 4 in which three heat maps from three AP's (AP1, AP2, AP3) are compared with the data collected for the positioning purpose. This values corresponds with the location marked with vertical line. To find users location the distance between collected data sample and heat map values must be calculated in the RSSI space. This can be done by using an euclidean distance:

$$\bar{d}_{\mathrm{RSSI}} = \sqrt{\sum_{i=1}^{n} (\mathrm{RSSI}_i^s - \mathrm{RSSI}_i^{hm})^2} \tag{2}$$

or Manhattan distance:

$$\bar{d}_{\mathrm{RSSI}} = \sum_{i=1}^{n} \left| \mathrm{RSSI}_i^s - \mathrm{RSSI}_i^{hm} \right| \tag{3}$$

where:
n is the number of access points (or heat maps), RSSI_i^s is collected RSSI value for i-th AP and RSSI_i^{hm} is the RSSI value read from i-th heat map. After calculating this distance in each node of the heat map, the cumulative heat map of distances can be created (Fig. 5). The minimum value of this heat map corresponds to user location.

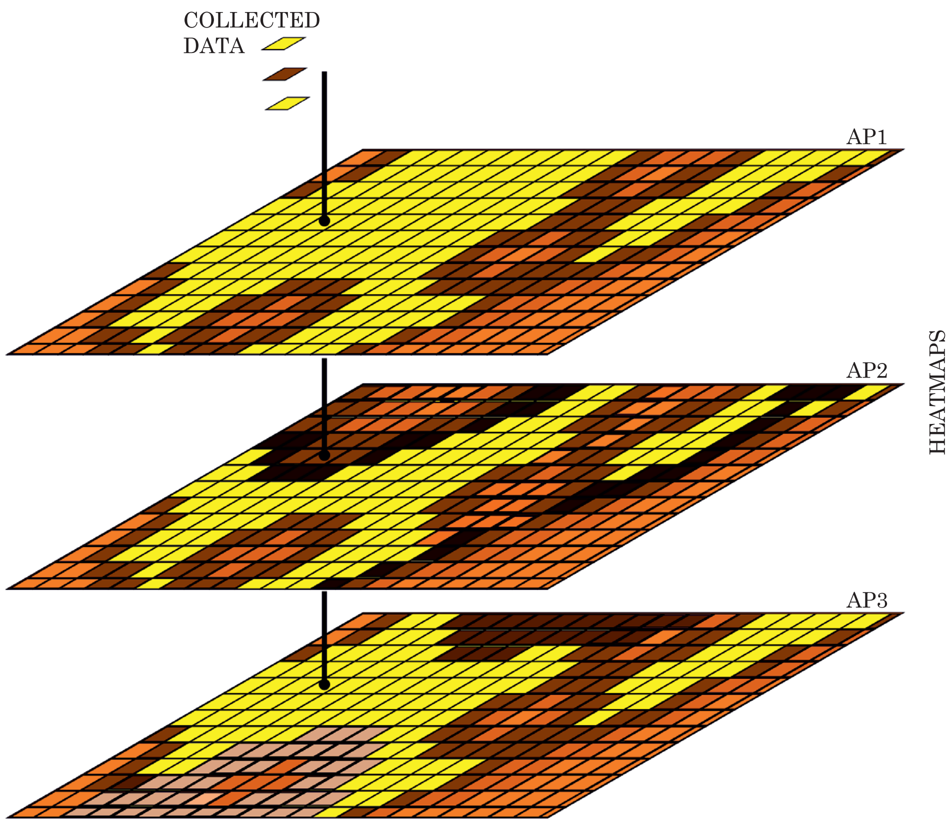

Fig. 4. The idea of heat-map comparison

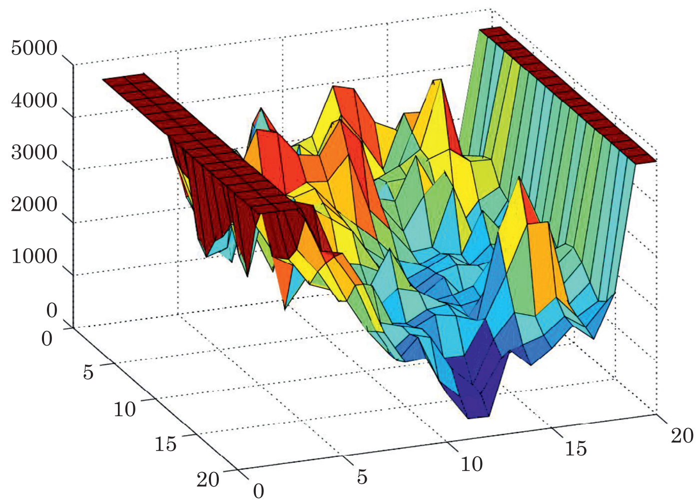

Fig. 5. Cumulative heat map

RSSI corrections

The positioning using the RSSI fingerprint is suitable for use in the indoor environment. In the modern society, hand-held devices (like smartphones or tablets) are very popular and can be easily adapted for such positioning system. Built-in Wi-Fi and Bluetooth transceivers can read the RSSI value and dedicated software can calculate users position. Hand-held device is usually held in front of the user. This is causing the attenuation of the signal from AP-s that are behind a user (since this signals does not propagate through human body) (CHEFFENA 2012). This can cause the situation in which the signal to one or more AP is read incorrectly, which can lead to incorrect result of positioning. The differences between the value of RSSI read in the line of sight and obstructed by user at different distances are depictede in Figure 6.

The measurements for Figure 6 were made in the multipath free environment, and still the difference in signal strength varies from 10 to 20 dBm. To investigate if this effect is caused by the human body attenuation only, or this shows combined effect of human body attenuation and antenna radiation pattern, two measurements were made. In the first one only the smartphone was rotated, and RSSI data to a single AP was collected. Results are shown in Figure 7. Looking at this figure, there is no regular attenuation at any angle, only noise is visible.

The second measurement involved rotation of a person holding a smartphone in front of him. The results are depicted in Figure 8. In this figure the maximum attenuation at about 70 degrees is noticeable, which is exactly at the oposite side of the AP. It means that this effect is caused by attenuation and/or diffraction of signal caused by a human body.

To mitigate this effect, a modelling of the intensification of signal strength can be introduced. The model should intensify the signal coming from the azimuths on the back side of a user. The formula for the correction term should reflect changes in the signal strength with respect to the angle between the user and an AP. It should amplify the readings for the APs that are behind user and leave the signal from the line-of-sight APs unchanged. Our proposal is the use of the following function:

$$\mathrm{RSSI}_{\mathrm{corrected}} = \mathrm{RSSI}\left(-\frac{k}{\sigma}\, e^{\frac{-(\alpha-180)^2}{2\sigma^2}} + 1\right) \tag{4}$$

where α is a user to AP azimuth, σ parameter describes the width of the intensification curve and k is a parameter describing the amount of „flattening" of the signal behind user. In the presented examples the parameters were chosen empirically to be $\sigma = 35$ and $k = 6$. The readings presented in the examples were made using WiFi signal. Linksys E900 Wireless-N300 router was used as a source of the signal and Samsung Galaxy S4 as a receiver. The results of application of this model to RSSI readings presented in Figure 8 is presented in Figure 9. Figures 10 and 11 depicts the correction function in different conditions (with different k parameter).

It can be noticed that the attenuation caused by a human body obstructing the line of sight is corrected, and only a certain amount of noise is visible. From the empirical experiments made by authors, the σ parameter fixed at the value of 35 is correct for any person and environment. The k parameter depends on the environment and should be derived during the process of fingerprint creation.

Conclusions

The method to mitigate the influence of the human body (of a person holding a smartphone) on RSSI reading is presented in this paper. Since the attenuation varies with rotation angle, neglecting this effect can cause different positioning results for a person standing in the same place depending on his or her heading. Application of the proposed formula, gives the possibility to mitigate this effect which can lead to improvement in positioning accuracy and reliability.

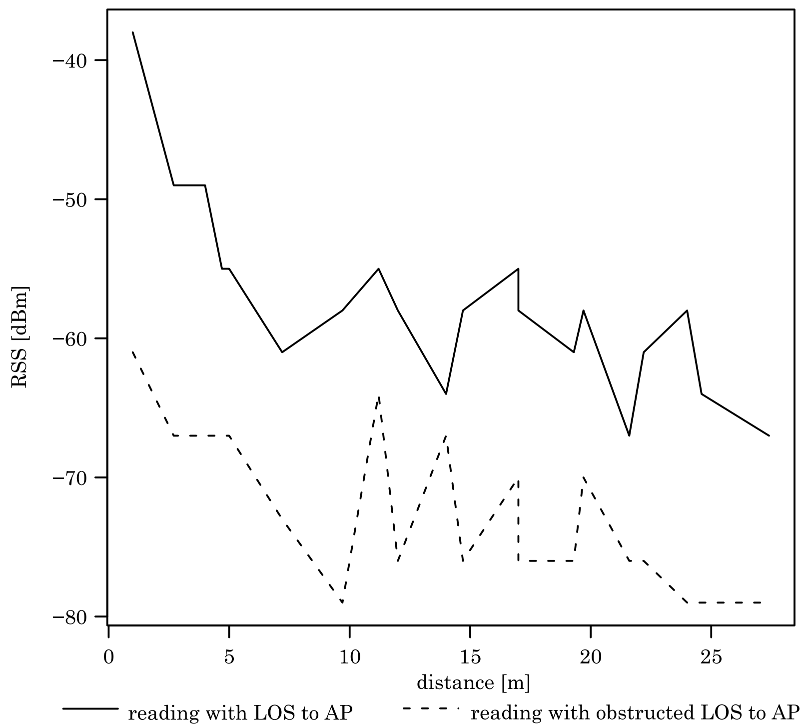

Fig. 6. Influence of a human body obstructions on the signal strength measurement

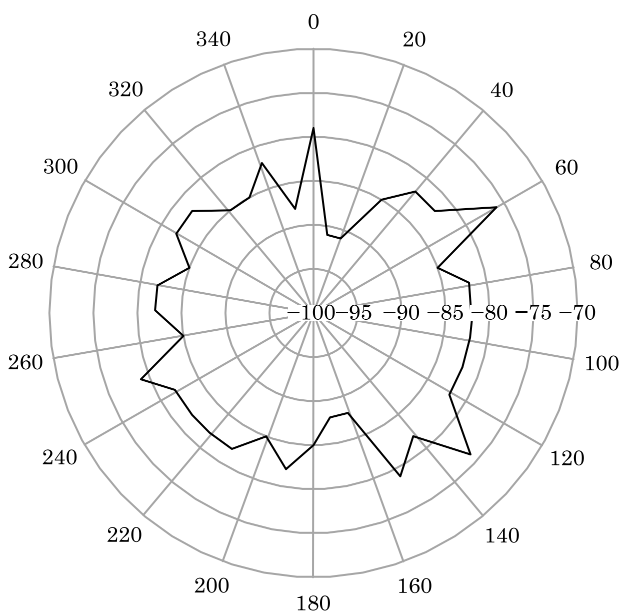

Fig. 7. RSSI [dBm] vs smartphone rotation

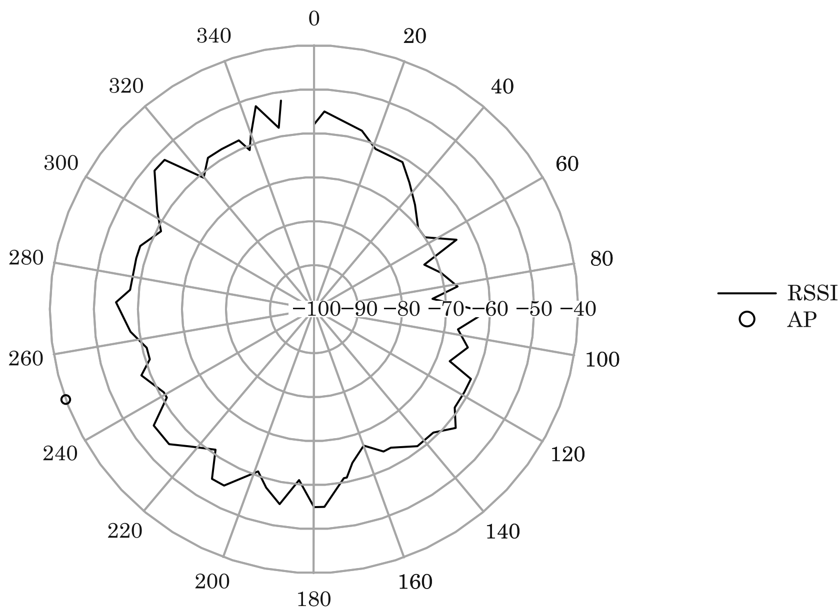

Fig. 8. RSSI [dBm] vs person with smartphone rotation

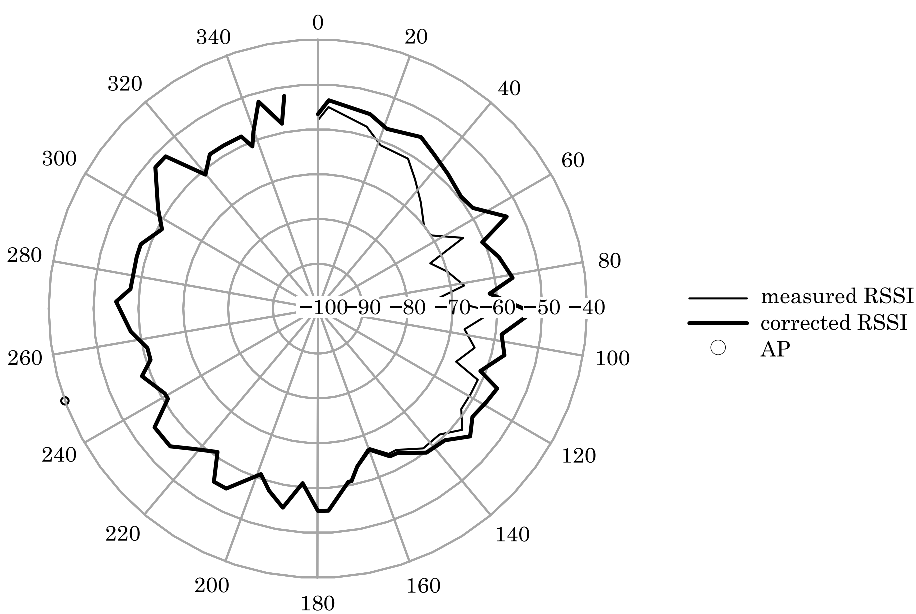

Fig. 9. Results of application of correction function (small room with AP behind the wall $k=6$)

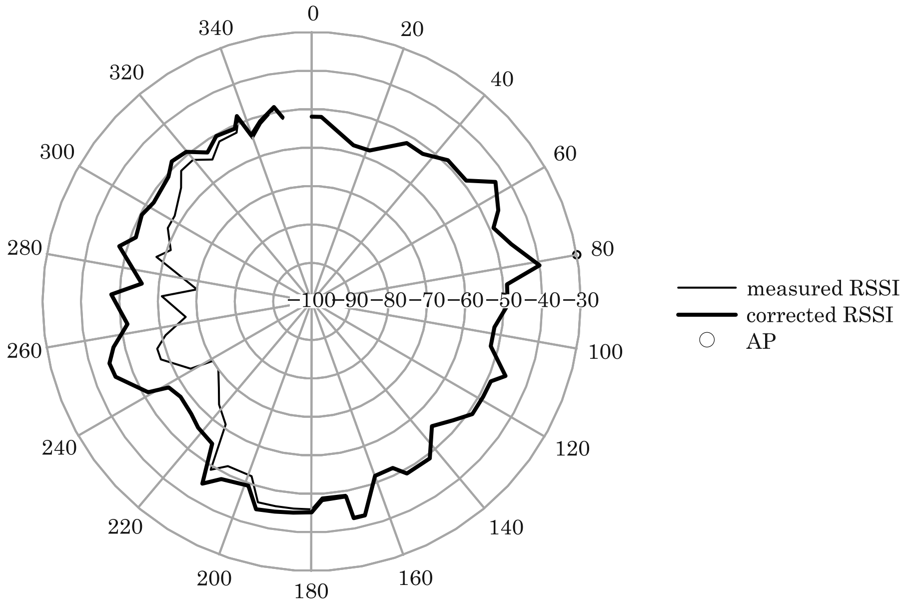

Fig. 10. Results of application of correction function (small room with AP in it k=8)

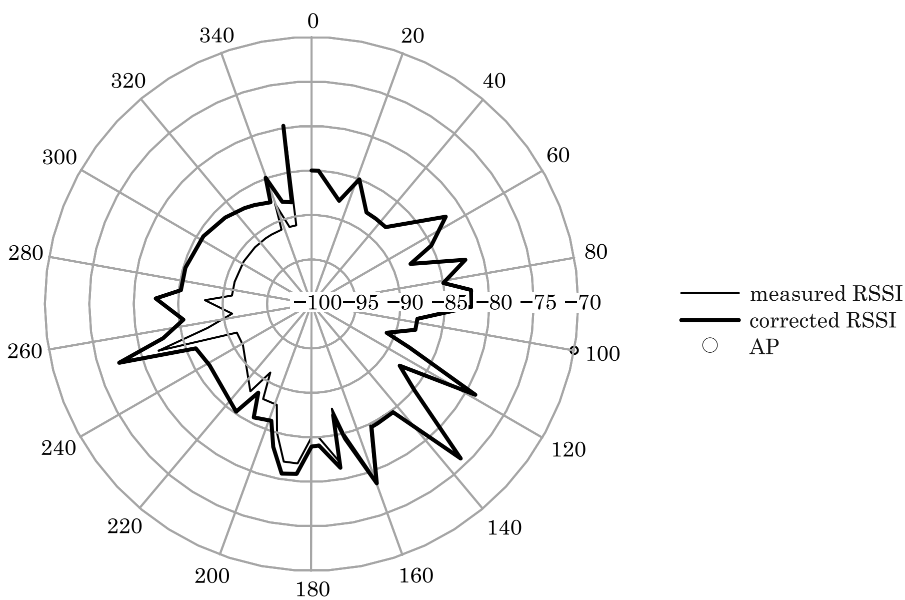

Fig. 11. Results of application of correction function (corridor with AP far from transceiver and behind the wall k=3.5)

The major disadvantage of this approach is that the location of an AP must be known in order to calculate the azimuth. This is only possible when using dedicated infrastructure. In the case when existing infrastructure, with unknown APs location is to be used, a method of finding the location of APs needs to be introduced. This issue will be a topic of further work and papers.

References

BARDWELL J. 2004. *You Believe You Understand What You Think I Said... The Truth About 802.11 Signal And Noise Metrics*. A Discussion Clarifying Often-Misused 802.11 WLAN Terminologies. Technical Report.

CHEFFENA M. 2012. *Physical-statistical channel model for signal effect by moving human bodies*. EURASIP Journal on Wireless Communications and Networking, 2012: 77. DOI: 10.1186/1687-1499-2012-77.

FRIIS H.T. 1946. *A Note on a Simple Transmission Formula*. Proceedings of the IRE, 34(5): 254–256. DOI: 10.1109/JRPROC.1946.234568.

GANSEMER S., GROSSMANN U., HAKOBYAN S. 2010. *RSSI-based euclidean distance algorithm for indoor positioning adapted for the use in dynamically changing WLAN environments and multi-level buildings*. International Conference on Indoor Positioning and Indoor Navigation (IPIN), IEEE, p. 1–6.

IEEE Standards Association. 2012. IEEE Std 802.11TM-2 2012. https://standards.ieee.org/findstds/standard/802.11aa-2012.html.

KUO W.H., CHEN Y.S., JEN G.T., LU T.W. 2010. *An intelligent positioning approach: Rssi-based indoor and outdoor localization scheme in zigbee networks*. International Conference on Machine Learning and Cybernetics (ICMLC), 6: 2754–2759.

SHEN X., WANG Z., JIANG P., LIN R., SUN Y. 2005. *Connectivity and RSSI based localization scheme for wireless sensor networks.* Advances in Intelligent Computing, 3645: 578–587.

Technical Sciences, 2016, 19(2) 129–138

UNIWERSYTET WARMIŃSKO-MAZURSKI W OLSZTYNIE

Quarterly peer-reviewed scientific journal
ISSN 1505-4675
e-ISSN 2083-4527
TECHNICAL SCIENCES
Homepage: www.uwm.edu.pl/techsci/

MATHEMATICAL MODELS FOR SPECIALIZED AND SENSORY NETWORKS OF WIRELESS ACCESS

***Oleksandr Tymchenko*[1], *Michał Zelyanovsky*[2], *Karolina Szturo*[1,3], *Oleksandr O. Tymchenko*[2]**

[1] Department of Safety Engineering
University of Warmia and Mazury
[2] Ukrainian Academy of Printing, Lviv
[3] Lodz University of Technology

Received 17 January 2015, accepted 24 May 2016, available online 25 May 2016.

Key words: sensor networks, mathematical model, topology control.

Abstract

This article reviews and compares the special features of specialized wireless and sensor networks. The components of a mathematical model of existing specialized wireless and sensor network are also available for review, particularly: wireless channel models, signal propagation models and communication graph models, etc. The need for a topology control mechanism in wireless and sensor networks is also explained.

Introduction

Specialized wireless networks include networks in which there is no fixed infrastructure and whose network topology may change with time. A wireless sensor network is a particular case of a specialized network that all the devices in such a network are homogeneous. Multilink transmission is used in both types of networks (HAENGGI et al. 2009, JERUCHIM et al. 2000, JOHNSON, MALTZ 1996, RAPPAPORT 1996). The following table summarizes the features of two related types of networks.

Correspondence: Oleksandr Tymchenko, Katedra Inżynierii Bezpieczeństwa, Uniwersytet Warmińsko-Mazurski, ul. Oczapowskiego 11, 10-719 Olsztyn, phone: 89 524 61 25.

Table 1

Features of specialized wireless networks and wireless sensor networks

Specialized wireless networks	Wireless sensor networks
Heterogeneous devices	homogeneous devices
Mobile nodes	stationary (quasi-stationary nodes)
Multilink transmission is optional	multilink transmission is needed in most cases
Geographically located network	

Problems

One of the most difficult aspect in determining the model of wireless network is that, yet complete enough. The simplicity will allow simulating and displaying the theoretical results and completeness should be provided so that such a model could be applied in practice. Let us consider the components of mathematical models for the specialized and sensor wireless networks (RAPPAPORT 1996).

The wireless channel

We introduce the following notation:
- u,v – a pair of wireless nodes,
- P_r and P_t – power of received and transmitted signals, respectively,
- β – sensitivity threshold,
- PL(u, v) – transmission losses (losses on tract).

A direct wireless connection exists if, and only if, $P_r \geq \beta$. The value of β depends on many factors, including the parameters of the transceiver and the data rate. The higher the data rate is, the higher β is:

$$P_r = \frac{P_t}{PL(u,\ v)} > \beta.$$

The presence of a wireless channel between u and v can be foreseen, if PL(u, v) are known. A modeling of losses on a tract is the most difficult task. The mechanisms of regulation of a signal's propagation can be divided into three categories: reflection, diffraction and dispersion.

Distribution of signal and losses on a tract

Losses on a tract are modeled in accordance with distribution of signal. There are a few models of distribution of signal, thus for every partial case it is possible to create a unique model.

Let's denote:

- G_t, G_r – amplification factors of the transmitting and receiving antennas, respectively,
- λ – wavelength,
- L – losses are on a tract.

1. Direct visibility. This model is the simplest and is used when there are no obstacles between a transmitter and receiver. Consequently:

$$P_r(d) = \frac{P_t \times G_t \times G_r \times \lambda^2}{(4\pi)^2 \times d^2 \times L},$$

using symbol

$$\frac{G_t \times G_r \times \lambda^2}{(4\pi)^2 \times L} = C_f,$$

we have:

$$P_r(d) = C_f \times \frac{P_t}{d^2}.$$

From the last equality, we see that the coverage area in the model of distribution on direct visibility is a circle of radius $d = \sqrt{C_f \times P_t}$.

2. Dual-beam model

Accept h_t, h_r heights of receiver and transmitter antennas from the ground (Fig. 1).

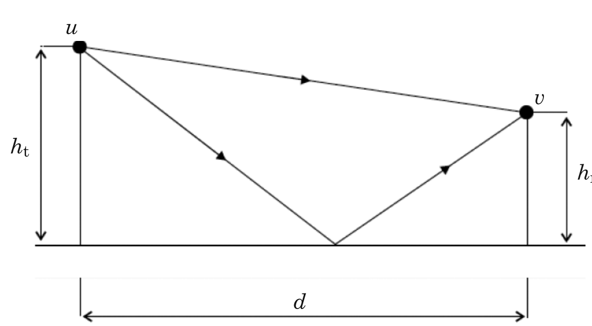

Fig. 1. In the dual-beam model, the signal spreads in two ways – the direct and the reflected beam from the ground

Then, assuming that horizontal distance $d = \sqrt{h_t \times h_r}$, have: $P_r(d) = C_f \times \dfrac{P_t}{d^4}$.

3. A model with logarithmic dependence on distance (a model for a heterogeneous or anisotropic environment).

Let's consider a model for a heterogeneous environment. It can be seen from above that the radius of coverage area $r \propto \sqrt[\alpha]{P_t}$. The value of α is defined experimentally for the different type environments, some partial cases are shown in the following table.

Table 2

Value of h defined for the different type of environments

Environment	Value of α
Open space	2
City	2.7–3.5
Inside the building, direct visibility	1.6–1.8
Inside the building, direct visibility is missing	4–6

Source: SANTI (2012).

Such a model assumes only the average value of the accepted power which may significantly differ from the peak values. Therefore, to predict the variability of the wireless channel, so-called probabilistic models of distribution are used. They are divided into 2 classes: large-scale (large range) and small-scale (small range). The latter are also called models of the multi-beam signal fading or simply fading.

Important among the large-scale models is the model with the logarithmic normal shading, where losses on a tract are modeled by changing with a random value which has logarithmic normal distribution in circumscription $\frac{P_t}{d^{\alpha}}$. The most important model of a signal's fading is Rayleigh's model (TYMCHENKO, ZELYANOVSKIY 2008).

There are also models for ultra-broadband connection, narrowband connection, and unlicensed frequency bands for industry, science and medicine (ISM, Industrial, Scientific and Medical band), where for losses on tracts the models of control points are used: $L(d) = \begin{cases} 40.2 + 20 \times \log(d) & d \leq 8m \\ 58.3 + 33 \times \log(d/8) & d > 8m \end{cases}$

For networks which are intended for the use inside of a building, there is a model of losses on a tract considering the walls and ceilings, for networks which work in open terrain and also in forest, the investigated losses effect is in a letter.

Communication graph

A communication graph determines the topology of the network, namely, the set of connections, which nodes could be used for communication.

Let us introduce the denotation in the topology graph:
– N – the set of wireless nodes,
– d – number of considered dimensions, in our case $d = 1, 2, 3$,
– l – side of square region,
– R – connected region in which the nodes are placed, $R = [0, l^d]$,
– $L(u)$ – reflection u in R, given in d-measurable coordinates,
– T – time interval of realization (a set of modeling moments),
– t -time flow.

Function L: $N \to R$ connects each node with its location inside R. In the case of mobility of wireless nodes, we have the function L: $N \times T \to R$ defines the plurality of d-measurable coordinates, giving the location of $\forall\ u \in R$ and $\forall\ u \in T$. Thus, the d-measurable wireless specialized mobile network is represented by a pair Md = (N, L).

In the function of determination of coverage area for M_d there is a certain function *RA,* that indicates for every element u in N a value of transmission range $RA(u) \in (0,r_{\max})$, $r_{\max}$ – the maximal distance of the node's transmission u. Determination of part R, whose information can be correctly accepted is possible on the basis of information about $r \in (0,r_{\max})$ and the amount of measurement of network d. For a one-dimensional network, it is a segment with a length centered at u, for a two-dimensional network it is a circle of radius r with center u and in the case of three-dimensional networks (e.g. a network of underwater sensors located at different depths) – the ball of radius r centered at u (Fig. 2).

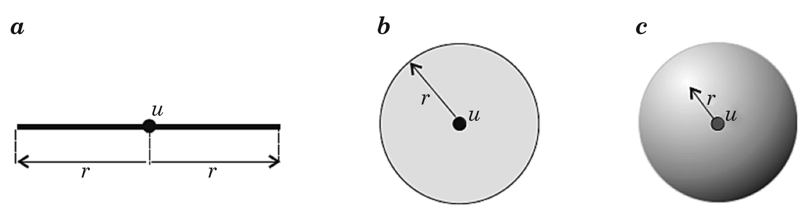

Fig. 2. Measurements for a wireless network in which a modeling is conducted: a – it is a one-dimensional area, b – two-dimensional, c – three-dimensional areas accordingly

Having a network M_d = (N, L) and function RA, we introduce the notion of communication graph, displayed with the function RA on M_d at the moment of time t. It is an oriented graph $G_t = (N,E(t))$, where a directed rib $[u, v]$, that belongs to the plural of ribs $E(t)$, exists then and only after

$RA(u) \geq \delta(L(u,t),L(v,t))$, $\delta(L(u,t),L(v,t))$ – Euclidean distance between u and v at time t. In other words, a connection between u and v is possible when, and only after, the distance between nodes at most RA(u) at the moment of time t. In the case of the existence of rib [u, v], v is the neighbor of the first link for u. Wireless connection is considered symmetric, if $(u,v) \in E_t$ and $(v,u) \in E_t$. In this case u, v are symmetric neighbors.

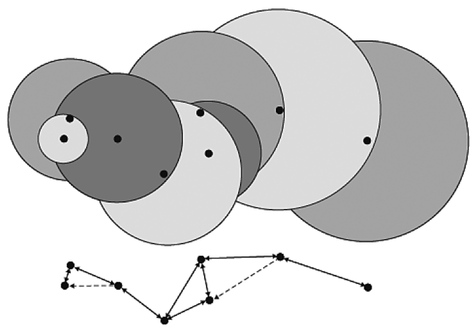

Fig. 3. Example of a wireless network communication graph

Determination of the coverage area at maximal measurement power, such that RA(u) = $r_{\max}$ for $\forall u \in N$ means that every node transfers at maximal power. We call the resulting communication graph, the graph of maximal power. Such a graph presents all the possible connections between nodes in a network.

Determination of the coverage area depends on time t, if a communication graph is coherent in time t, i.e. if there is at least one oriented route between any two nodes.

Determination of the coverage area at which all the nodes have the same radius of transmission r, $r \in (0,r_{\max})$ called r-homogeneous or simply homogeneous, if a value *of* r is not important. It should be noted that the communication graph, generated by homogeneous determination of coverage area for every node, is non-oriental, as $(u,v) \in E_t \Leftrightarrow (v,u) \in E_t$.

Energy consumption is one of the most important metrics in wireless sensor networks. Let α – a degree of losses on a tract. Having some determination of coverage area RA for a network $M_d = (N, L)$, we can say that expenses of energy c on providing RA determined as:

$$c(RA) = \sum_{u \in N} RA(u)^{\alpha}$$

Models of mobility of the specialized wireless networks

Most models of mobility provide movement without obstacles, as it simplifies modeling considerably.

1. RWP – Random Waypoint model – a node randomly selects some point and moves to it on a line. When a mobile node arrives at the destination point, it makes a pause, then elects the coordinates of a new destination point and continues movement (VERDONE et al. 2008).

2. RDM – Random direction model – a node randomly selects a direction and rate of movement. Once the node reaches the boundary of spreading of R, there are a few variants of subsequent actions (ZELYANOVSKIY, TYMCHENKO 2008):

– to choose a new direction and speed and continue movement to the bound R;

– to „reflect" from the bound R and continue movement;

– modification: a node moves in select direction some casual time t, and then changes direction and speed of movement.

3. Model with Brownian movement – in such a variant, movement in steps is used which are chosen randomly, thus the parameters of every next step depends on the previous. An example of a model of Brownian motion is a model using three parameters:

– P_{stat} _ the probability that movement is absent all of the time,

– P_{move} – the probability that a node will move during a current interval of time,

– m – model speed of a node at the present moment of time.

If a node moves during some interval of time i, then its position at the moment of time $i+1$ is determined randomly in a square with a side $2 \times m$ centered at the current node position.

4. Model considering geography – in this case nodes move along predefined ways. Previous nodes are placed in such ways and begin to move on a given scheme. At the crossroads (if such are present) nodes randomly choose the direction and speed of further movement.

5. A model with mobility of groups. From all set of nodes N, a certain subset of leaders is elected $N_l \subset N$, thus $|N_l| \subset |N|$. All other nodes randomly choose a leader and move after him. The leader may use one of the above models.

Topology control of wireless networks

Topology control aims to control the set of connections between pairs of nodes in the network to facilitate and enable the general one-or two-way messaging between all nodes in the network (SANTI 2006).

The theory of topology control is closely connected with the theory of the connectivity of a communication graph network. The primary goal of topology control in the protocol stack is the search for optimal coverage area for each node in the network to provide the required properties of all networks (energy consumption, total coverage area, the lifetime of the network). Optimality may be, for example, the full connectivity of nodes with minimal radiated power of nodes. If all nodes have the same parameters of radiation power (in the case of homogeneous networks – sensor networks), then we can talk, in particular, about the critical radius of coverage area (CTR).

Critical coverage area

Critical coverage area *rc* for providing of compendency of communication graph, is the minimum value of radius of coverage area r, $r \in (0,r_{\max})$ such that at r-homogeneous determination of the coverage area, a communication graph is coherent. P. Santi in JERUCHIM et al. (2000) proved that *rc* in some network $M_d = (N, L)$ corresponds to the longest rib of Euclidean carcass of communication graph G (EMST – Euclidean Minimum Spanning Tree). The difficulty is that for the distributed system (which is a specialized or sensory wireless network) transmission of global (from the point of view of the whole network) knowledge about the coordinates of every node to each of the nodes is surplus and requires plenty of messages, that, in the same queue, leads to losses of power. The latter affects such parameters as the lifetime of the network.

Topology control consists of determining and deleting nodes of the network from a communication graph which are ineffective in terms of energy consumption.

In Figure 4 the two-dimensional communication graphs of network ($d=2$) are represented. On the left all possible values of r_c are shown. On the right we can see the real value *of* r_c, which provides the compendency of graph.

$d = 2$; CTR = 1.5

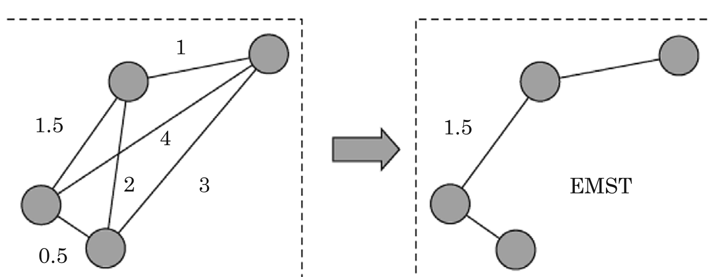

Fig. 4. Communications graph and critical coverage area

In JERUCHIM et al. (2000) it is shown that, in terms of energy consumption, it is appropriate to use multilink messaging over short distances rather than trying to convey a message without the relaying. Multilink transmission of information can also increase the network capacity, i.e. the number of simultaneously working devices in it as message transmissions over long distances creates interference for nodes that are located in a coverage zone, which leads to the retransmission of messages or even makes the communication impossible in the area of such difficult conditions.

Conclusions

Recently, scientific resources have focused on modeling signal transmissions in cellular systems or broadcast communications (JOHNSON, MALTZ 1996). But the models for cellular communication cannot be applied in the case of sensor networks because, first of all, it is typical of the placement of a pair of nodes (base station, mast antenna) at a high distance from the ground, while in the case of the sensory network, all nodes can be located on the ground (for example, right in the grass) or be attached to the walls of the building. Therefore, the direction of modeling of specialized and sensor wireless networks, as well as personal range networks is actively developing and only beginning to emerge a complete model for networks of this class. The considered components are rapidly improving, and there are new specifications to them. The correct creation of the model and its verification ensure successful operation of the network, reducing the time expenses of modeling and debugging and allows the efficiency of the existing network to be improved.

References

HAENGGI M., ANDREWS J.G., BACCELLI F., DOUSSE O., FRANCESCHETTI M. 2009. *Stochastic geometry and random graphs for the analysis and design of wireless networks*. IEEE Journal on Selected Areas in Communications, 27(7): 1029–1046.

JERUCHIM M.C., BALABAN P., SHANMUGAN K.S. 2000. *Simulation of Communication Systems*. Second Edition. Kluwer Academic/Plenum, New York.

JOHNSON D.B., MALTZ D.A. 1996. *Dynamic source routing in ad hoc wireless networks*. In: *Mobile Computing*. Eds. T. Imielinski, H. Korth. Chapter 5, pp. 153–181. Kluwer Academic Publishers, Invited paper.

RAPPAPORT T.S. 1996. *Wireless Communications*. 1st edn. Upper Saddle River, Prentice Hall, New York.

SANTI P. 2006. *Topology control in wireless ad hoc and sensor networks*. ACM Computing Surveys (CSUR), 37(2): 164–194.

SANTI P. 2012. *Mobility models for next generation wireless networks: ad hoc, vehicular and mesh networks*. John Wiley & Sons Ltd., New York, p. 23.

TYMCHENKO O., ZELYANOVSKIY YU. 2008. *Methods and protocols of data exchange of sensory networks of*. The Collection of Scientific Works, IPME NAS of Ukraine, 46: 176–183.

VERDONE R., DARDARI D., MAZZINI G., CONTI A. 2008. *Wireless Sensor and Actuator Networks: Technologies, Analysis and Design*. Elsevier, London.

ZELYANOVSKIY YU., TYMCHENKO O. 2008. *Intellectual system for wireless specialized sensory and networks of the personal radius of action: software and hardware platform of node of wireless network of*. Design and information technologies. The Collection of Scientific Works, IPM NAS of Ukraine, 49: 185–193.

Technical Sciences, 2016, 19(2) 139–149

Quarterly peer-reviewed scientific journal
ISSN 1505-4675
e-ISSN 2083-4527
TECHNICAL SCIENCES
Homepage: www.uwm.edu.pl/techsci/

EFFECT OF THE HEIGHT OF THE DELIVERY WATER ON PERFORMANCE OF WATER RAM

Dariusz Grygo

Department of Mechanical and Machine Design
University of Warmia and Mazury in Olsztyn

Received 27 December 2015, accepted 24 May 2016, available online 25 May 2016.

Key words: ram water, test stand, equations of performance.

Abstract

The main aim of this article is to develop mathematical equations of the performance stream ($\dot{V}_c$) of a water ram with regard to the height of water delivery (h_c). The study was performed on the sample water ram of my own design mounted on a specially designed test stand. The content of the article is divided into two parts. The first part describes a generalized equation on the base formulae used historically to determine the performance of the water ram. The second part presents the results of research and summarizes the mathematical equations determining the streams performance ($\dot{V}_c$) according to the height of water delivery (h_c). In conclusion the article makes interpretations of the results. The motivation to approach these issues stems from the question: How much will the performance of the water ram has on the ability to set a receiver tank at different heights?

Introduction

The water ram is a kind of water pump to lift water to higher levels (H_d) than the height of the water source (H) (Fig. 1). The ram pump action is based on the use of kinetic energy of water flowing through the device. The water supply source can be any flow for example: river, stream, lake, etc. It is only important that the flow must provide adequate water ($Q + Q_w$), to create an appropriate water hammer necessary to further correct its work (MOHAMMED 2007, CLARKE 1900, WATT 1975).

Correspondence: Dariusz Grygo, Katedra Mechaniki i Podstaw Konstrukcji Maszyn, Uniwersytet Warmińsko-Mazurski w Olsztynie, ul. Oczapowskiego 11, 10-719 Olsztyn, e-mail: dariusz.grygo@gmail.com

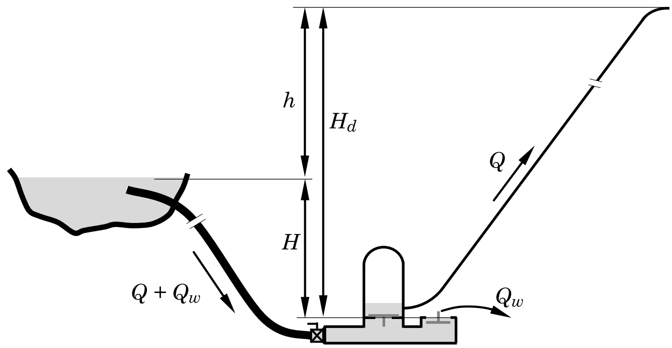

Fig. 1. Scheme of water ram describes Rankine and D'Aubuisson methods

Analyzing the history of water rams can find information about their efficiency. The efficiency can be described by the following methods (TAYE 1998, MOHAMMED 2007, WATT 1975, LANSFORD, DUGAN 1941, JONG 2015, CALHOUN 2003, DERKOR 2014, ZOLLER 2015, CLARKE 1900, MARUCHIN, KUTIENKOW 2014):

– Rankine method:

$$E = \frac{Q \cdot H_d}{(Q + Q_w) \cdot H} \tag{1}$$

– D'Aubuisson

$$E = \frac{Q \cdot h}{(Q + Q_w) \cdot H} \tag{2}$$

where:
E – is the efficiency of the hydram,
Q – is the pumped flow [l/min],
Q_w – is the wasted flow [l/min],
h – is the pump head above the source [m],
H – is the supply head above the waste valve opening [m],
H_d – is the total head above the waste valve opening = $(H+h)$ [m].

The main aim of this work is to define the mathematical relationship that makes it possible to determine the impact of the delivery height of the water (H_d) on the performance (Q) of the water ram (Fig. 1).

Other relationships allow for an accurate calculation of the performance (Q) of the water ram and all of its opportunities to lift water taking into account parameters such as: the volume of the air chamber, the height of the water source (H_d) and the height of water delivery (H) described in detail in part one of a series of articles about water rams, GRYGO D. et al.: *Performance characteristics of water rams*. The study was performed on a simple water ram of my own design mounted on a specially designed test stand.

The motivation for the study is to improve machinery and equipment so that their action is based on unconventionally by using renewable energy for devices that can be used in the household e.g. to improve its energy balance, free delivery of water, land irrigation, the watering of animals, etc.

The work presented the results of performance and mathematical equations of performance for three options: 1. h_s = 5 m, 2. h_s = 4 m, 3. h_s = 3 m (see Fig. 2). The summary presents the interpretation of these results.

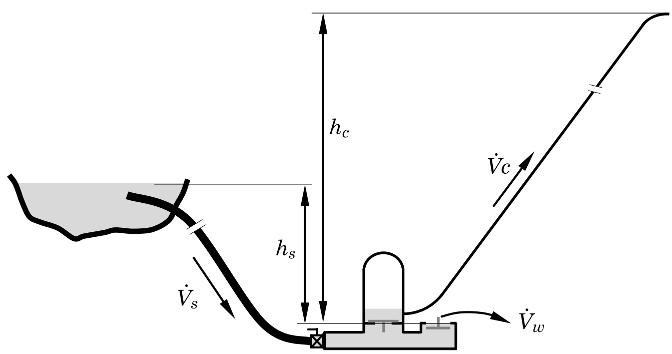

Fig. 2. Installation scheme of water ram

Performance equations

Performance measurements of the water ram were carried out for three heights of different water supply (3, 4 and 5 m) and for eight ranges of water lifting (in ranges of 5 to 16 m). For each configuration three measurements were made. The performance was determined by the „mass flow" rate method. The method of mass flow rates was selected due to high accuracy and a short measuring time.

To measure the amount (weight) of water collected in holding tanks (*1* and *2*) (Fig. 3) the measuring system uses a force sensor Axis type FA200 (*3* and *4*) with the maximum rate measuring 200 [N] (~ 20 kg) with a measurement accuracy of ±0.05. Following suspension of the holding tanks the sensors were reset so as to indicate only the weight of the water. Knowing the weight of water accumulated in holding tanks and its temperature determined its mass. The water temperature was measured by an electronic sensor with an accuracy of 0.1°C.

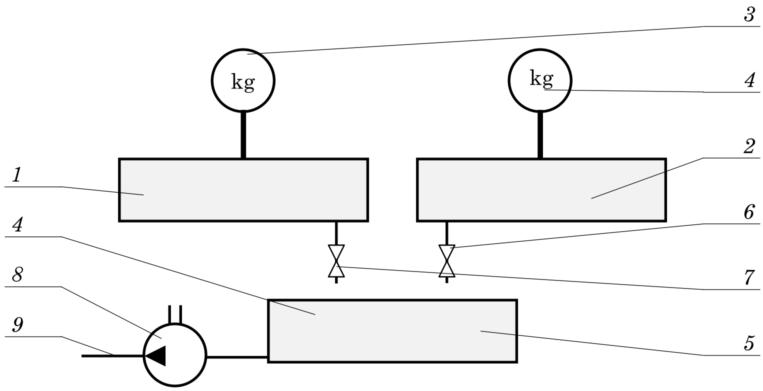

Fig. 3. The measuring system

For this purpose, an electronic thermometer was used with readout system of internal and external temperatures by means of a probe. A thermometer was placed in a shaded area approximately 0.5 m of the water tank and the probe placed inside the tank.

The water ram worked for measurement for about 15 minutes. At this time the impulse valve was regulated to obtain the stability of all the system parameters. After this period a redirection the outflow water ($\dot{V}_w$ and $\dot{V}_c$), according to the measuring tanks (*1* and *2*) was made. The water collected for 180 s, over time delivered volume readings. After readings valves were opened (*6* and *7*) and the water flowed into the tank (*5*). From there via the electric water pump (*8*) to the main supply tank. It was important to mount the electric pump so that the amount of water in the system was constant. The settings of the parameters were as follows: h_s = 3, 4 and 5 m, the temperature was 15.0°C and the volume of the air chamber of the water ram was 3 dm^3. In Table 1, 2 and 3 the average results of three measurements are shown. Figures 4, 5 and 6 show the water flow rate in graphical form for a particular configuration and in Figures 7, 8 and 9 show mathematical equations in a graphical form.

Table 1

Measurement results h_s = 5 [m]

h_c [m]	$\dot{V}_c$ [dm^3/180 s]
10	2.856
11	2.239
12	1.480
13	0.677

Table 2

Measurement results h_s = 4 [m]

h_c [m]	q_c [dm^3/180 s]
10	2.829
11	2.290
12	1.453
13	1.425
14	0.844

Table 3

Measurement results h_s = 3 [m]

h_c [m]	q_c [dm^3/180 s]
6	3.532
7	3.386
8	2.834
9	2.093
10	1.618
11	1.238
12	0.369

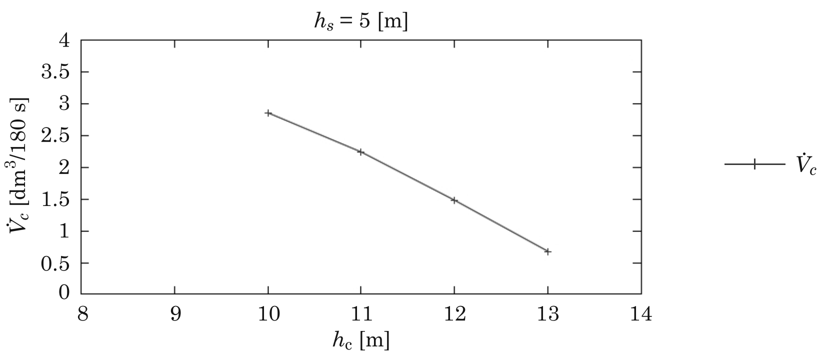

Fig. 4. The stream of water flow rate for h_s = 5 m

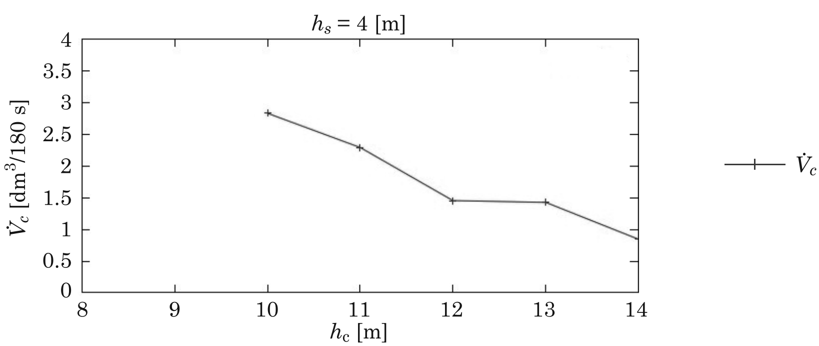

Fig. 5. The stream of water flow rate for h_s = 4 m

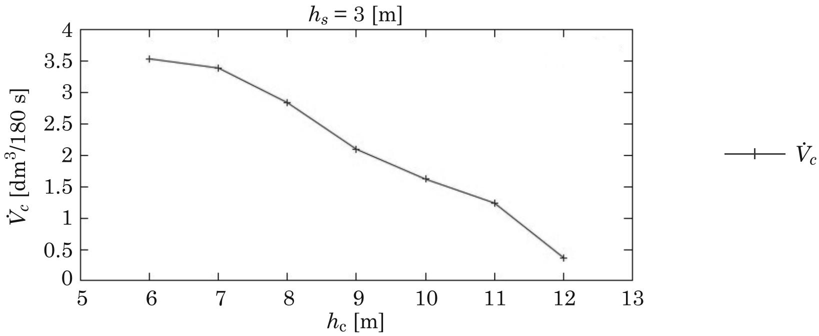

Fig. 6. The stream of water flow rate for $h_s = 3$ m

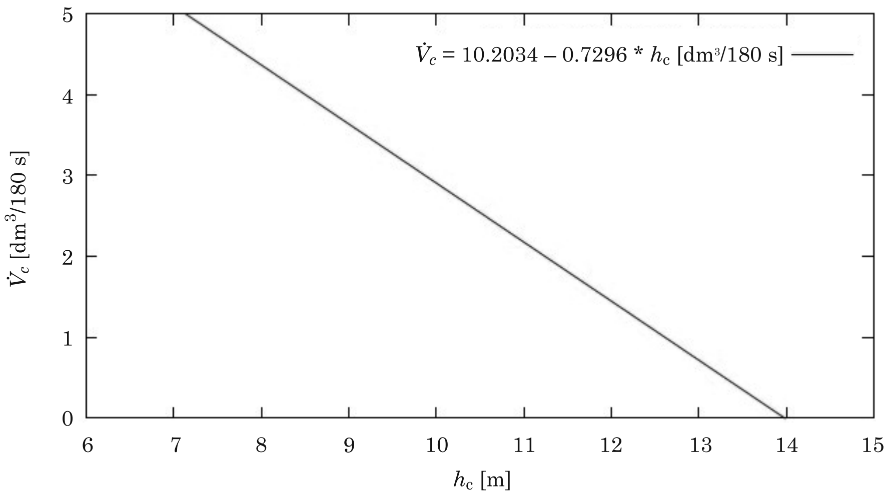

Fig. 7. The regression equation graph 6

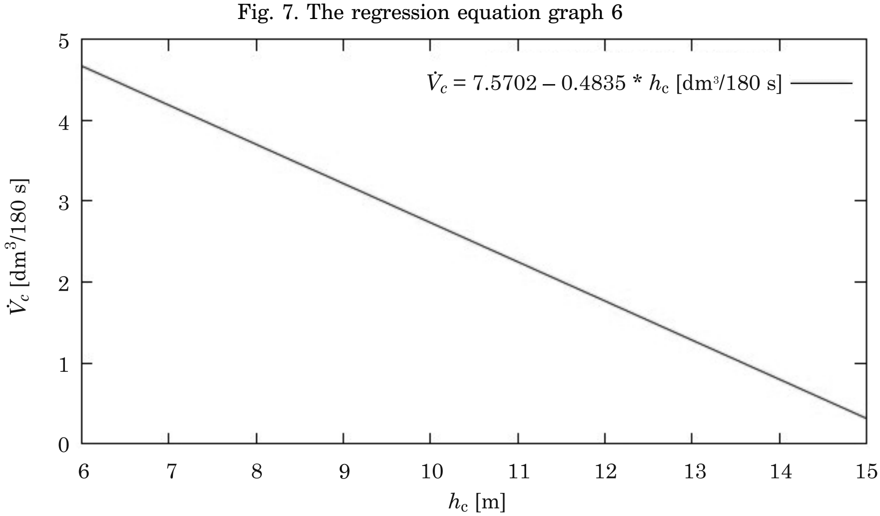

Fig. 8. The regression equation graph 7

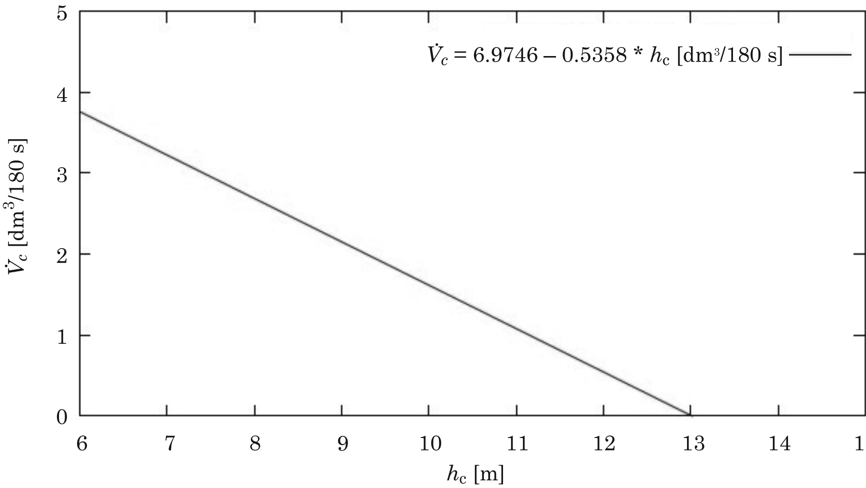

Fig. 9. The regression equation graph 8

The results were verified statistically using regression analysis. The regression analysis was used to determine the nature of the relationship between the dependent variable ($\dot{V}_c$) and the independent variable (h_c) for stochastic models describing the relationship:

$$\dot{V}_c = f(h_s) \tag{3}$$

was selected using the regression line (RABIEJ 2012, LUSZCZEWICZ, SLABY 2008). Guided by the principle that physical relationships often occur in simple mathematical forms (PRZESTALSKI 2009) and that reality can be successfully described by several models (OSOWSKI 2007), tested the function of the following forms:

$$Y = \xi_0 + \xi_1 X_1 + \xi_2 X_2 + \xi_3 X_3 \tag{4}$$

for the calculation of statistical procedures, I used package Statistica PL. v10 (STANISZ 2007). The hypotheses verified H_0, that the structural parameters of the equation were insignificantly different at zero ($\alpha_i = 0$). In a case where $p(F) \geq \alpha$ there was no reason to reject the hypotheses H_0 and when $p(F) < \alpha$ rejected in a favor of the alternative hypotheses H_1 ($\alpha_i \neq 0$). The results of the statistical calculations and regression equations shown in the appropriate Tables 2, 4 and 6.

Table 4

The results $h_s = 5$ m

Variable	Average value	Standard deviation	The coefficient of variation [%]
Lift height water h_c [m]	11.50	1.118034	9.72
Water flow rate $\dot{V}_c$ [m^3/180 s]	1.81	0.817115	45.07

Verification of the hypothesis about the significance of the coefficients of regression equations
H_0: The regression coefficients are zero
H_1: Not all of the regression coefficients are equal to zero
Test results:

The percentage of variation explained	99.66
Multiple correlation coefficient	0.998
The standard deviation of the residues	0.067562

The critical region right-hand
The level of significance = 0.05
The calculated value of statistics $F_{(1;2)} = 583.0918$
The level of probability test $p = 0.0017$
H_0 should be rejected in favor of the alternative hypothesis H_1

Table 5

The results $h_s = 4$ m

Variable	Average value	Standard deviation	The coefficient of variation [%]
Lift height water h_c [m]	12.00	1.414214	11.79
Water flow rate $\dot{V}_c$ [m^3/180 s]	1.77	0.7002688	39.74

Verification of the hypothesis about the significance of the coefficients of regression equations
H_0: The regression coefficients are zero
H_1: Not all of the regression coefficients are equal to zero
Test results:

The percentage of variation explained	94.69
Multiple correlation coefficient	0.973
The standard deviation of the residues	0.209071

The critical region right-hand
The level of significance = 0.05
The calculated value of statistics $F_{(1;3)} = 53.4816$
The level of probability test $p = 0.0053$
H_0 should be rejected in favor of the alternative hypothesis H_1

Table 6

The results $h_s = 3$ m

Variable	Average value	Standard deviation	The coefficient of variation [%]
Lift height water h_c [m]	9.00	2.000000	22.22
Water flow rate $\dot{V}_c$ [m^3/180 s]	2.15	1.082022	50.26

Verification of the hypothesis about the significance of the coefficients of regression equations
H_0: The regression coefficients are zero
H_1: Not all of the regression coefficients are equal to zero
Test results:

The percentage of variation explained	98.06
Multiple correlation coefficient	0.99
The standard deviation of the residues	0.178107

The critical region right-hand
The level of significance = 0.05
The calculated value of statistics $F_{(1;5)} = 253.3488$
The level of probability test $p = 0.0000$
H_0 should be rejected in favor of the alternative hypothesis H_1

The equation of performance (*h_s* = 5 m)

The linear regression. General information: number of observations = 4, adopted significance level = 0.05.

The regression equation:

$$\dot{V}_c = 10.2034 - 0.7296 \cdot h_c \tag{5}$$

The equation of performance (*h_s* = 4 m)

The linear regression. General information: number of observations = 5, adopted significance level = 0.05.

The regression equation:

$$\dot{V}_c = 7.5702 - 0.4835 \cdot h_c \tag{6}$$

The equation of performance (*h_s* = 3 m)

The linear regression. General information: number of observations = 7, adopted significance level = 0.05.

The regression equation:

$$\dot{V}_c = 6.9746 - 0.5358 \cdot h_c \tag{7}$$

Summary

The main aim of this work is to define the mathematical relationship that allows determination of the impact of the height of water (h_c) on the performance ($\dot{V}_c$) of water ram. Analyzing the results obtained during the performance of the test it was able to determine the equation of variation of functions for each specified of height of delivery. The first model (h_c = 5 m) is the most suited (99.66 percent of the explained variations) while two other models have proved to be well matched (94.69 and 98.06 percent of the explained variations). It was shown that the relationship for the model:

– First, that at the average height of water delivery (h_c) equals 11.5 m the performance is 1.81 dm^3/180 s. From the obtained mathematical data (regression equation) shows that by increasing the height of water delivery by 1 m will reduce the performance about 0.7296 dm^3/180 s and will be equal to 1.08 dm^3/180 s;

– Second, that at the average height of water delivery (h_c) equals 12.0 [m] the performance is 1.77 dm^3/180 s. From the obtained mathematical dependence (regression equation) it shows that by increasing the height of water delivery by 1 [m] it will reduce performance of 0.4835 dm^3/180 s and will be equal to 1.29 dm^3/180 s;

– Third, that at the average height of water delivery (h_c) equals 9.0 m the performance is 2.15 dm^3/180 s. From the obtained mathematical dependence (regression equation) it shows that by increasing the height of water delivery by 1 m it will reduce the performance by 0.5358 dm^3/180 s and will be equal to 1.62 dm^3/180 s.

References

CALHOUN J. 2003. *Home built hydraulic ram pumps.* http://www.homepower.com/how-ram-pump-works (access: August 2014).

CLARKE J.W. 1900. *Hydraulic rams ther principle and construction.* B.T. Batsford. https://archive.org/details/hydraulicramsth03clargoog (access: August 2014).

FURZE J. 2012. *Compendium in hydraulic ram.* University of Aarhus. Faculty of Political Science. http://www.slideshare.net/Fatin62c/compendium-in-hydraulic-rampumps (access: August 2014).

How does hydraulic ram work. 2014. Derkor. Without Fuel or Electricity. Pumping 24 hour per day. http://www.rampumps.net/face/20120410150106.html (access: March 2014).

JONG P. 2015. *Hydraulik rams.* Delf University of Technology.

LANSFORD W.M., DUGAN W.G. 1941. *An analytical and experimental study of the hydraulic ram.* Bulletin of the University of Illinois, XXXVIII(22), Engineering Experiment Station, Bulletin Series No. 326.

LUSZCZEWICZ A., SLABY T. 2008. *Statistics from the computer package Statistica PL. „Theory and Applications”.* CH Beck, Warszawa.

MARUCHIN W., KUTIENKOW W. 2013. *Nowe źródło niewyczerpanej czystej energii o dużej mocy: taran hydrauliczny – solidnie zapomniana stara myśl*. http://www.pinopa.republika.pl/Tarpend_pl.html (access: November 2013).

MOHAMMED S.N. 2007. *Design and Construction of a Hydraulic Ram Pump*. Leonardo Electronic Journal of Practices and Technologies, 11: 59–70.

OSOWSKI S. 2007. *Modelowanie i symulacja układów i procesów dynamicznych*. OWPW, Warszawa.

PRZESTALSKI S. 2009. *Elementy fizyki, biofizyki i agrofizyki*. Wydawnictwo Uniwersytetu Wrocławskiego, Wrocław.

RABIEJ M. 2012. *Statystyka z programem Statistica*. Helion, Gliwice.

Sequences of Operation. 2014. Meribah Ram Pump. Proved & Reliable. Water Pumping Solution. Retrieved from http://www.meribah-ram-pump.com/index.php?id=29 (access: January 2014).

STANISZ A. 2007. *Przystępny kurs statystyki z zastosowaniem STATISTICA PL na przykładach z medycyny*. Tom 1. *Statystyki podstawowe*. Tom 2. *Modele liniowe i nieliniowe*. Tom 3. *Analizy wielowymiarowe*. StatSoft Polska, Sp. z o.o., Kraków.

TAYE T. 1998. *Hydraulic ram pump*. Journal of the ESME, II(1).

WATT S.B. 1975. *A manual on the hydraulic ram for pumping water*. Intermediate Technology Publications Ltd. http://www.watersanitationhygiene.org/References/EH_KEY_REFERENCES/WATER/Water%20Pumping/Ram%20Pumps/Hydraulic%20Ram%20Pump%20Manual%20(ITDG).pdf (access: January 2014).

ZOLLER F. 2015. *Hydraulic ram pumping in rural community development*. Rijswijk University of Professional Technical Education, Durban.

Technical Sciences, 2016, 19(2) 151–164

UNIWERSYTET WARMIŃSKO-MAZURSKI W OLSZTYNIE

Quarterly peer-reviewed scientific journal
ISSN 1505-4675
e-ISSN 2083-4527
TECHNICAL SCIENCES
Homepage: www.uwm.edu.pl/techsci/

EXPERIMENTAL INVESTIGATIONS OF CAVITATING FLOWS IN A VENTURI TUBE

Agnieszka Niedźwiedzka, Wojciech Sobieski

Department of Mechanics and Basics of Machine Construction, Faculty of Technical Sciences, University of Warmia and Mazury in Olsztyn

Received 5 March 2015, accepted 18 April 2016, available online 6 May 2016.

Key words: cavitation, test rig, Venturi tube.

Abstract

This article presents results of the experimental measurements of the cavitation phenomena in a Venturi tube with water as the working medium. Three variants of such tube were tested. Angles of converging and diverging sections are equal to 45° and 45°, 30° and 60°, 45° and 60°, respectively. In every case the throat diameter is equal to 3 mm and the throat length to 6 mm. The average flow velocity ranges from 0.1 to 0.5 m/s. During measurements, the average flow velocity, upstream and downstream pressure and water temperature were recorded. Additionally, by the use of a high-speed camera and a simple digital camera, information about the size and the shape of the bubble clouds for different flow conditions was collected. The aim of the article is data acquisition for the further numerical analyses. The experimental runs executed for this paper are to help provide more information about this type of flow, since numerical modeling of the cavitation phenomena in Venturi tubes is still very difficult and in many cases even quantitative agreement is impossible to obtain.

Introduction

Cavitation phenomena could be defined as the evaporation process of a liquid in areas where the local pressure drops below the saturation pressure. This pressure depends in turn on the temperature of the liquid. If the pressure increases (in space or in time), the vapour bubbles disappear. Cavitation is generally undesirable due to its negative consequences: erosion, noise, vibrations and energy losses (BAGIEŃSKI 1998).

Correspondence: Agnieszka Niedźwiedzka, Katedra Mechaniki i Podstaw Konstrukcji Maszyn, Uniwersytet Warmińsko-Mazurski, ul. Oczapowskiego 11, 10-736 Olsztyn, e-mail: agnieszka.niedzwiedzka.@uwm.edu.pl

In real-life applications, cavitation occurs even if the local value of the pressure is higher than the saturation pressure. Such state is due to the fact that in real fluids small bubbles of the non-dissolved gases exist. The presence of such bubbles (called nuclei) is observed for each kind of liquid it may cause a change in the tensile stress of the liquid, in terms of decreasing it. (BAGIEŃSKI 1998). The tensile stress for „clear" water (for temperatures in the 5–15°C range) reaches values of approximately 27 MPa and depends on the temperature of liquid. The increase of temperature translates into a drop of the value of tensile stress. The tensile stress is reduced to zero at approximately 374°C (KNAPP et al. 1970). Change in tensile strength may also change other material properties, which depend upon it: density, viscosity, surface tension and air content (NOSKIEVIČ 1969).

However, it is possible for cavitation to still occur, even in the absence of nuclei. The theory of liquid disturbance describes the phenomenon of homogeneous nucleation. This theory relates to the possibility of creating bubbles with critical dimensions in water without any nuclei. Liquids, considered at the molecule level, are in the dynamic state, which means that these molecules are in continuous motion. Through the motion of the molecules, empty spaces may be formed between them. Under favourable conditions, i.e. increase of temperature or/and drop of pressure, these spaces could turn into bubbles with critical dimensions (APFEL 1972).

The discovery of a new physical phenomenon in 1894, responsible for destruction of a ship propeller (REYNOLDS 1894), opened a new period in the world of technical science. The scale of negative after-effects of the appearance of unexpected vapour bubbles in water persuaded scientists to familiarize with the unknown phenomenon. The observations conducted in natural environment could not help to find the answer to many questions. The only way to shed light on the enigmatic phenomenon was an experiment. Experimental studies of cavitating flows are carried out until 1935 (HUNSAKER 1935). The story of Venturis as the object of the interests of scientists started in 1952 (RANDALL 1952). Since 1962, the experimental investigations of the flow inside Venturis have taken into account also the influence of cavitation (NUMACHI et al. 1962, NUMACHI, KOBAYASCHI 1964). The complex character of the cavitation phenomenon resulted in experimental studies of cavitating flow inside Venturis to be continued to this day (ABDULAZIZ 2014, DECAIX, GONCALVES 2013).

The main function of Venturis is a passive control of the mass flow rate. These devices are a common application in industry. The Venturis as an application can be found first in parts of hydraulic systems, where a constant mass flow rate is expected. Their big advantage is the assurance of an unchanging flow rate independent from the variable pressure in a chamber. Through these features, Venturis, as a precise tool, could be used as a flow meter (GHASEMMI, FASIH 2011). Their construction consists of three parts: a converging section (nozzle), throat, and a diverging section (diffuser). To the most essential features of Venturis, which have an influence on the mass flow rate and the flow character, belong the throat diameter, the throat length and the diffuser angle (ASHRAFIZADEH, GHASEMMI 2015). The broad applications of Venturi tubes support the simple form of the device. Additionally, their construction does not have any moving parts. Consequently, the production of Venturis does not require a lot of finance and these devices are characterized by high reliability. Therefore, use of these devices is on the one hand practical and on the other hand economical (GHASEMMI, FASIH 2011).

Venturi tubes, despite that they are a basic geometry, they are devices with varied shapes. In the classical form of Venturi tube presented in ISO 5167-1:2005, the angle of diverging section ranges from 7 to 15^o and the angle of converging section is 21^o. Scientists analysed also other shapes of Venturi tubes. NUMACHI et al. (1962) investigated in 1962 Herschel Venturi-tube. This tube is characterised by a sharper converging angle and is also the current research object. Brinkhorst et al. presented in 2015 the results of numerical simulations of cavitating flow in Herschel Venturi tube. They analyzed the influence of geometry parameters on the stability of the mass flow rate. Additionally, the authors made the same investigations for toroidal Venturi nozzle (ISO 9300:2005) which is distinguished by a radius in the converging section and a direct transition to the diverging section.An important type of a Venturi tube is an asymmetric Venturi (BARRE et al. 2009, RODIO, CONGEDO 2014, CHARIERRE et al. 2015). BARRE et al. (2009) presented double optical probe measurements and numerical studies based on the code Fine^{TM}/Turbo and a barotropic approach. Rodio and Congedo prepared a stochastic analysis of cavitating flow. CHARIERRE et al. studied an aperiodic cavitation pocket in an asymmetric Venturi using chosen homogeneous models.

The main aim of the investigations of the cavitation phenomenon is to build new simulation models for different kinds of Venturi tubes using the homogeneous approach.The motivation to begin such investigations relate to the cavitation phenomena in Venturi tubes was the fact that the current available and most popular cavitation models are still too poor for such flows. Results from numerical modeling are too different from observations even on the qualitative level. According to the literature, the prediction of the cavitation phenomenon in the Venturi tubes in one of the most difficult cases and further investigations in this field are needed (PALAU-SALVADOR et al. 2007). For this reason, the Venturi tubes are often the subject of research of cavitating flows (BAYLA et al. 2009, TAMHANKAR et al. 2014, BRINKHORST et al. 2015). Despite widespread interest of scientists in this field, having a large number of different shapes for Venturi tubes impedes finding the expected experimental results for the chosen shape. For the mentioned study, recording the best accuracy of the Venturi tubes performance in experimental measurements is necessary. For this purpose, a new test rig was designed and built, which is presented in this article.

The article has the following structure: the first part is devoted to acquaint the reader with the design assumption. Knowledge of the validation process of the numerical models enables the reader to understand the detailed construction of the test rig. The description of the test rig, which is the second part of the article, starts with the history of investigation of cavitating flows at the Faculty of Technical Sciences and presents a comparison between the old and the new version of the test rig. After the introduction, a diagram of the device and the detailed presentation of the most important components follows. The next step of the article is the overview of the technical data and the description of the typical measurement process. The third part of the article is presentation of the capabilities of the experimental investigation of cavitating flows using the new test rig. The article ends with conclusions on the results obtained.

Assumptions

There are three basic approaches to integrate numerical fluid analyses with experiments (SOBIESKI 2013). The first approach (Fig. 1*a*) supposes only one-way interaction of experimental data with numerical analyses (CFD – Computational Fluid Dynamic). However, during creation of the simulation model it may happen that the experimental data proves to be insufficient or its quality will be too low. There is no possibility to repeat the investigation, so the results of the numerical simulations could be incorrect. The second approach (Fig. 1*b*) submits a correction to the previous version. The experiment can be repeated, if it is necessary, which translates in an improvement of the compatibility of the results between the real case and the virtual model. The disadvantage of this approach are time and cost needed for the repetition of the experiment. Besides, in some cases the experiment cannot be performed again. The best way to integrate the experimental and numerical investigations is the application of the following methodology (Fig. 1*c*): first, the preliminary numerical model is created. Then the experiment is planned and performed taking into account the knowledge about requirements of the numerical model. Finally, the preliminary numerical model is corrected and calibrated. In the current investigation, this methodology is applied, therefore at the beginning of investigations, the preliminary numerical model was created.

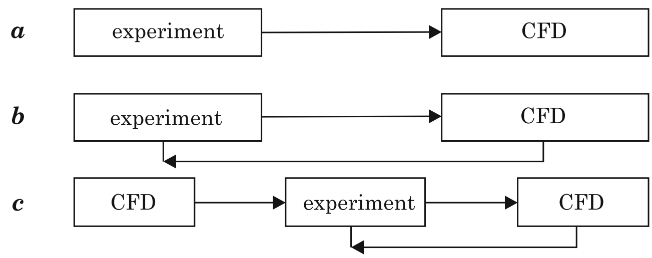

Fig. 1. Basic approaches to integrate numerical fluid analyses
Source: SOBIESKI (2013).

The data for numerical fluid simulations can be divided into three groups: geometry data, data defining the kind of fluid and information about the boundary conditions. The geometry data is necessary for mesh preparation. The rule for this case is as follows: the simpler geometry of the grid, the easier the meshing process will be and a shorter calculation time will be required. The data describing the physical medium includes information about the density and viscosity of the fluid. Since the analysed case concerns water, only its temperature has to be known. The temperature is an important parameter for cavitation phenomenon because it can change details the saturation pressure. For this reason, the experimental measurements should be performed with a constant temperature. There are three methods to establish the desired temperature. The first method assumes use of cold water and fast measurements. In the second approach the measurement may be performed after a time in which the system achieves the state of the thermodynamic equilibrium (the temperature will be constant). The third method assumes the automatic control of the temperature. This solution is the most convenient. The last set of information concerns boundary conditions. These terms should be understood as flow parameters. These parameters can be included in the simulation model in two ways. The first way assumes introducing information about the inlet velocity and outlet pressure. In the second method, information about the total inlet pressure and the dynamic inlet pressure should be used. In this case is important to enter the additional data about the reference values. The presented test rig meets the design assumptions.

Laboratory setup and methods

Test rig

The idea of experimental and numerical investigations of cavitation in hydraulic systems started at the Department of Mechanic and Basics of

Machine Construction at the Faculty of Technical Sciences of the University of Warmia and Mazury in Olsztyn between 2002 and 2004. The first test rig was created for the purpose of investigating cavitating flows. Using this test rig, photos were taken of the cavitation cloud behind the cavitation inducer and vibroacoustic analyses on the basis of the noise measurements in the flow were conducted (SOBIESKI 2004, 2005).

In 2010, this prototype was replaced with a new test rig (Fig. 2), which is directly intended for performing experiments of turbulent and cavitating flows, as well as many other flow phenomena. The device was made within the framework of the project TECH 2010. In comparison with the prototype, the new test rig was improved and has a few advantages. Some of these advantages are: having an inter alia with smaller dimensions, having the ability of motion using the wheels, automatic acquiring and saving of the signal from all sensors, direct displaying of the data, simple control of the flow velocity and the liquid temperature, as well as the independence from the connection to the water mains.

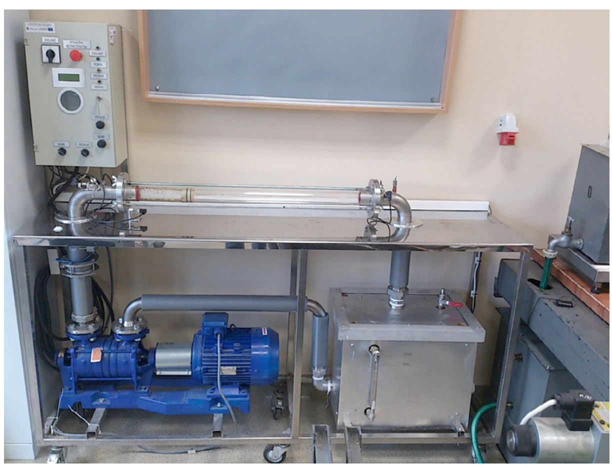

Fig. 2. The test rig from 2010

The scheme of the test rig is presented in the Figure 3. The whole device weighs approximately 115 kg. Its weight with water increases to approximately 195 kg. The test rig is 190 cm in height, 50 cm in width and 180 cm in length. The independence from the connection to the water mains is ensured by the hydraulic system with closed water circulation. The used self-priming pump up to 10 bar is suitable for liquids with the temperature not exceeding 110°C, density not exceeding 1300 kg/m^3 and viscosity not exceeding 150 mm^2/s. The maximum permissible size of impurities in form of indelible solid particles is

0.5 mm. The pump can obtain a maximum efficiency at level of 7 m^3/h, which translates into a linear velocity of water in the cavitation chamber of 1 m/s. A motor having a power of 5.5 kW is used as a drive to the self-priming pump.

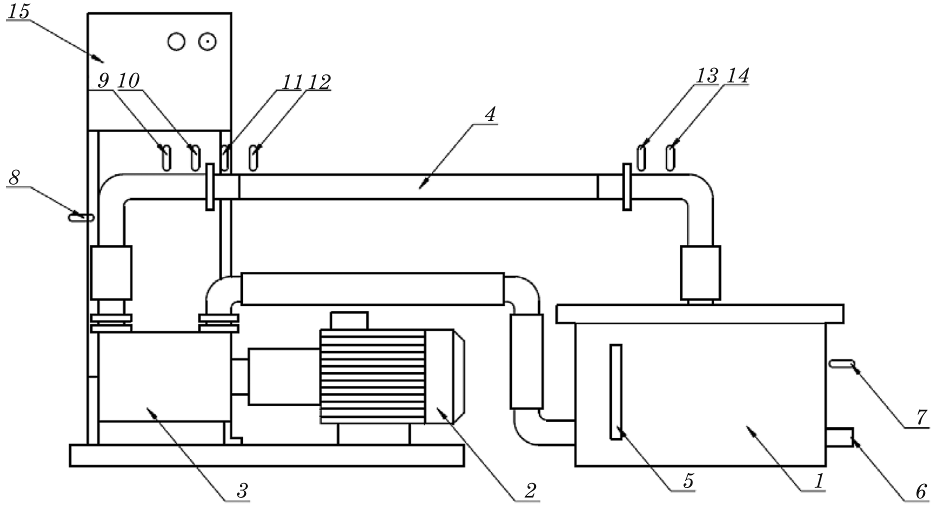

Fig. 3. The diagram of the test rig from 2010: *1* – water tank, *2* – motor, *3* – water pump, *4* – cavitation chamber, *5* – water indicator, *6* – heater, *7* – water level sensor, *8* – velocity inlet sensor, *9* – pressure inlet sensor, *10* – temperature inlet sensor, *11* – proximity sensor of the chamber, *12* – additional proximity sensor, *13* – pressure outlet sensor, *14* – temperature outlet sensor, *15* – control panel

The test rig is equipped with seven sensors that can work with temperature below 100°C and humidity below 50%. The measurements can be started, when the external temperature is between 0 and 40°C. The sensor of water level in the water tank is located in the right wall. The sensor is placed about 26 cm above the tank bottom, which corresponds to 46 l of liquid. It is the minimum safe level at which the water pump can be started. The direct control of filling level is enabled through the water indicator. The last sensors, placed below the tabletop, give information about the linear fluid velocity. To reduce the fluctuations of the signal, a filter with time constant of nine seconds was applied. Consequently, the data in display are delayed with regard to the correct flow.

The most interesting part of the test rig, i.e. the cavitation chamber, is placed above the tabletop. The plexiglas pipe has the internal diameter of 50 mm. The distance between both flanges is 1,000 mm. The cavitation chamber is only one of the variants of the system, which can be investigated using the presented test rig. The elbows of the inlet and outlet pipes are equipped with sensor sets, which include temperature and pressure sensors. The precision of each temperature sensor is 0.5°C. The pressure measuring range is between 0 and 10 bars. Additionally, on the right side of the left flange of the cavitation chamber, is placed a proximity sensor which has the aim to counteract switching on the hydraulic system in case there is a lack of the cavitation chamber.

The operating panel ensures the control of measurements. It has three flip switches to turn on power, motor and heater. Determination of temperature and percentage use of the motor is made by two independent potentiometers. The values of the given and the current temperature of water in the elbows of the inlet and outlet pipe and the percentage use of the motor are displayed on the LCD monitor. To other information, which can be found on the LCD monitor, belong the water pressure in the elbows of the inlet and outlet pipe and the linear velocity of the flow.

Venturis

In the analysed case, the cavitation inducers are three Venturi tubes (Fig. 4), which have their dimensions presented in the Figure 4. The angles of converging section were selected for the first Venturi as 45° (Fig. 4*a*), for the second 60° (Fig. 4*b*) and for the third 30° (Fig. 4*c*). The angles of diverging sections were selected as 45°, 30° and 60°, respectively. The throat has diameter of 3 mm and 6 mm length. The outside diameter of the Venturi tube is 50 mm. The Venturi is placed within 300 mm of the left edge of the cavitation chamber.

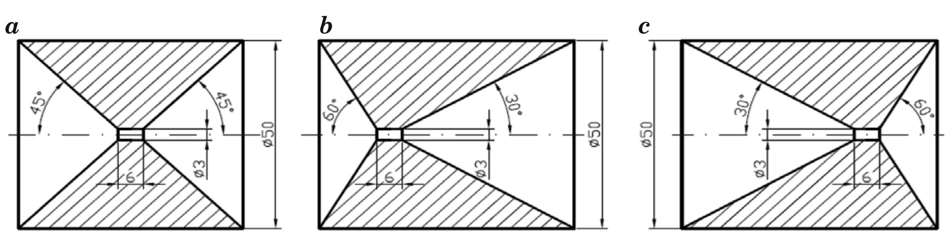

Fig. 4. Dimensions of the Venturi tube

Experimental method

To investigate the behaviour of the flow in the Venturi channel and the cavitation chamber an experiment has been conducted. In the experiment, the velocity flow and the temperatures and pressure at the inlet and outlet of the cavitation chamber have been measured. During the test, the value of the downstream pressure was constant; the value of the upstream pressure was variable. The data obtained in the experiment is presented in form of tables. The shapes of the cavitation cloud have been registered using a high-speed camera (Olympus i-SPEED TR, 1000 frames per second) and a simple digital camera (Nicon Coolpix P610).

Results and discussion

The first and main aim of experimental measurements is obtaining data for numerical analyses. The division of the essential information was presented in the first section of the article. The second part of the data, which concerns the physical medium, was reduced to the reference temperature. During tests of the laboratory device, the temperature was between 19 and 40°C.

Table 1

Results of experimental measurements for the first Venturi (Fig. 4*a*)

No.	u	T_1	T_2	p_u	p_q	p_u–p_q
	m/s	°C	°C	Pa	Pa	Pa
1	0.1	20.2	19.8	481,325	4.99	481,320
2	0.2	20.5	20.1	677,325	19.96	677,305
3	0.3	20.9	20.8	776,325	44.91	776,280
4	0.4	21.1	21.2	846,325	79.84	846,245
5	0.5	21.4	21.7	964,325	124.75	964,200

Table 2

Results of experimental measurements for the second Venturi (Fig. 4*b*)

No.	u	T_1	T_2	p_u	p_q	p_u–p_q
	m/s	°C	°C	Pa	Pa	Pa
1	0.1	31.1	32.1	657,325	4.99	657,320
2	0.2	32.6	32.9	757,325	19.96	757,305
3	0.3	35.6	36.1	1,022,325	44.91	1,022,280

Table 3

Results of experimental measurements for the third Venturi (Fig. 4*c*)

No.	u	T_1	T_2	p_u	p_q	p_u–p_q
	m/s	°C	°C	Pa	Pa	Pa
1	0.1	24.1	24.2	534,325	4.99	534,320
2	0.2	24.7	24.8	719,325	19.96	719,305
3	0.3	28	28	811,325	44.91	811,280
4	0.4	29.7	29.4	980,325	79.84	980,245
5	0.5	35.8	35.6	1,099,325	124.75	1,152,200

The last part of data includes boundary conditions, in other words, flow parameters. In case of cavitation simulation both ways of defining of flow parameters, velocity inlet – pressure outlet and pressure inlet – pressure outlet, are possible. All desired information are either displayed on the LCD monitor (average fluid velocity – u, inlet total pressure – p_u and outlet total pressure – p_d) or calculated based on this information (dynamic pressure – p_q, difference between the inlet total pressure and the inlet dynamic pressure $p_u - p_q$). In the tables 1–3 data from the experimental measurements is presented. Pressure in the outlet of cavitation chamber (p_d) has a constant value of 101.325 Pa.

From the data presented in the Tables 1–3 it is evident that the maximum average velocity at the inlet of the cavitation chamber is 0.5 m/s. In the case of the second type of Venturi, the maximum average value of the velocity achieves only 0.3 m/s. The temperature of the medium starts from 19°C and finishes before reaching 40°C. The total pressure at the inlet of cavitation chamber varies from about 4 bar (for the average velocity at the inlet equal to 0.1 m/s) to 10 bar (for 0.5 m/s). The differences between upstream total pressure and upstream average velocity for the analysed variants of Venturis are notable. For the upstream average velocity equal to 0.1 m/s the value of the upstream total pressure starts from 3.8 bar for the first type of Venturi, for the third type achieves value 4.33 bar and for the second 5.56 bar. The differences are visible in the whole of the experimental measurements. For the upstream average velocity of 0.3 m/s, the value of the upstream total pressure starts from 6.75 bar for the first type of Venturi, for the third type achieves value 7.1 bar and for the second 9.21 bar. Additionally, the maximum upstream average velocity for the second type of Venturi is only 0.3 m/s, which is a direct indicator that changes in the angles of Venturi influences the upstream velocity and upstream pressure. ASHRAFIZADEH and GHASEMMI (2015) indicate that changing of the diverging section angle does not affect the values of upstream pressure and velocity. However, the changes of the converging section angle are not without impact on these values.

The second aim of experimental measurements is obtaining data that is useful by post-processing. The test rig has not any instrumentation that would allow collecting data for validation process. The simplest and the most common method is evaluation of the intensity and size of the cavitation cloud based on photos. Photos can be made using a high-speed camera (Fig. 5–7) or even a simple camera (Fig. 8). Photos can be compared with distribution of vapour volume fraction in the chamber from numerical simulations. In the Figures 5*a*–5*e* are presented cavitation clouds for the first type of Venturi for five upstream velocities: 0.1, 0.2, 0.3, 0.4 and 0.5 m/s. For the velocity equal to 0.1 m/s, the cavitation cloud is only faintly visible. Increasing velocity leads

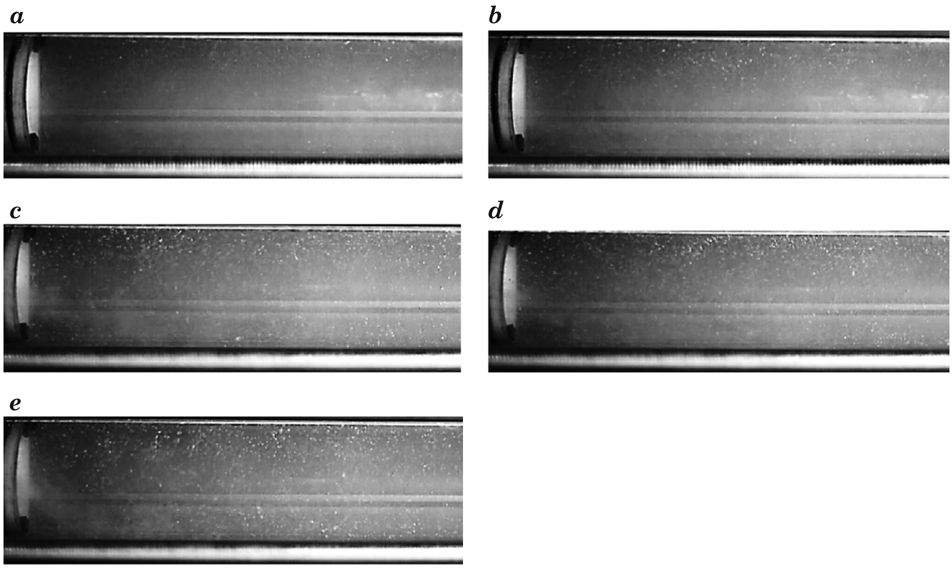

Fig. 5. Cavitation cloud at different velocities for the first type of Venturi: *a* – 0.1 m/s, *b* – 0.2 m/s, *c* – 0.3 m/s, *d* – 0.4 m/s, *e* – 0.5 m/s

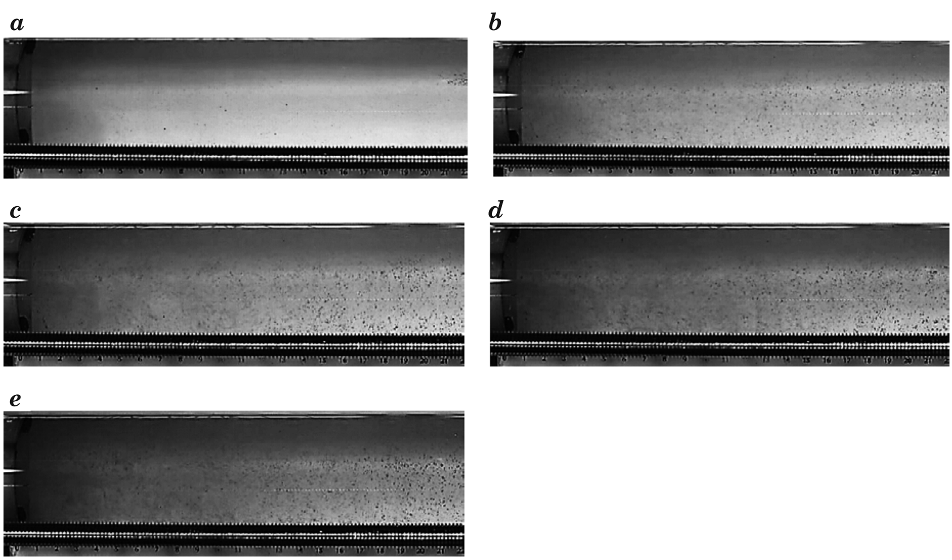

Fig. 6. Cavitation cloud at different velocities for the third type of Venturi: *a* – 0.1 m/s, *b* – 0.2 m/s, *c* – 0.3 m/s, *d* – 0.4 m/s, *e* – 0.5 m/s

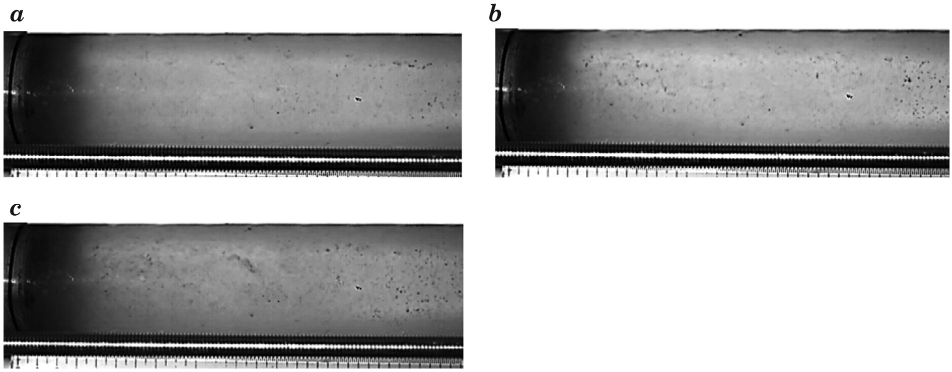

Fig. 7. Cavitation cloud at different velocities for the second type of Venturi: *a* – 0.1 m/s, *b* – 0.2 m/s, *c* – 0.3 m/s

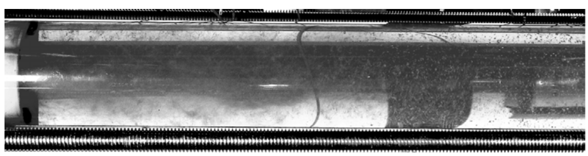

Fig. 8. Photo of cavitation cloud made using a simple camera

to clearer contours between the vapour bubbles and water. Starting from the 0.3 m/s velocity, it is visible that the stream of vapour bubbles after leaving of the diverging section heads for the downstream part of the cavitation chamber and then bounces upstream, forming a hook shape. Between the cavitation clouds for the first and the third type of Venturi (Fig. 6*a*–6*e*) there are many similarities. Among these a blurred shape of the cavitation cloud for the low upstream velocity (Fig. 6*a*) and the increasing of its intensity for higher velocities (Fig. 6*b*–6*e*). The difference between the analysed cavitation clouds is their shape. For the third type of Venturi, the cavitation cloud has no hook form anymore, but a slightly wavy line. The shape for a second type of Venturi is different from the above described (Fig. 7*a*–7*c*). A hook form or a slightly wavy line is no more visible. The cavitation cloud spreads to the whole volume of the cavitation chamber for each of the analysed upstream velocities. Increasing of the upstream velocity leads to increasing of the intensity of the cavitation cloud and its length.

Conclusions

Based on the experimental measurements the following concluding remarks can be made:

– Using the test rig, in objects like a Venturi tube, cavitating flow can be observed.

– The control range of the test rig is sufficient to obtain an intensive and broad cavitating cloud.

– Using the measuring system of the test rig, essential data about pressure and velocity at the inlet and outlet of the cavitation chamber and the water temperature can be obtained.

– Based on the experimental data and the dimensions of the cavitation chamber numerical models for the considered flow cases can be prepared. It means that the main aim of the experimental measurements is achieved.

– Use of the high-speed camera gives a qualitative observation of the intensity and extent of the cavitation cloud. The gathered results should be sufficient material to make comparisons between the experiment and numerical simulations. More over, as shown in the literature study, the most important in the case of Venturis is quality of the experimental and numerical data.

– Using a simple camera did not give enough good results in terms of quality. This method, which is simpler and more accessible, is only of auxiliary importance.

– The type of Venturi and flow parameters has influence on the intensity and extent of the cavitation cloud. In the considered investigation range three forms of cavitation cloud were observed: a hook form, a slightly wavy line and dispersed.

– Reconstruction of the right flow structure in numerical models will be probably the most difficult stage of the numerical simulations.

– A better quality of the experimental data can be achieved using Particle Image Velocimetry (PIV), but currently we do not have access to such measurement systems. To resolve this problem we will try to use an alternative method, which was developed in cooperation with the Department of Electrical and Power Engineering, Electronics and Automation, and will be presented in a future publication.

Acknowledgements

The authors want to thank Dr. Eng. Andrzej Anders for photos made using a high-speed camera.

References

ABDULAZIZ A. M. 2014. *Performance and image analysis of a cavitating process in a small type Venturi*. Experimental Thermal and Fluid Science, 53: 40–48.

APFEL R.E. 1972. *The tensile strength of liquids*. Scientific American, 227(6): 58–71.

ASHRAFIZADEH S.M., GHASEMMI H. 2015. *Experimental and numerical investigation on the performance of small-sized cavitating Venturis*. Flow Measurement and Instrumentation, 42: 6–15.

BAGIEŃSKI J. 1998. *Kawitacja w urządzeniach wodociągowych i ciepłowniczych*. Wydawnictwo Politechniki Poznańskiej, Poznań.

BARRE S., BOITEL G., ROLLAND J., GONCALVES E., FORTES PATELLA R. 2009. *Experiments and modeling of cavitating flows in venturi: attached sheet cavitation*. Europan Journal of Mechanics B/Fluids, 28(3): 444–464.

BAYLA A., AYDIN M.C., UNSAL M., OZKAN F. 2009. *Numerical modeling of venturi flows for determining air injection rates using fluent v6.2*. Mathematical and Computational Applications, 14(2): 97–108.

BRINKHORST S., VON LAVANTE E., WENDT G. 2015. *Numerical investigation of effects of geometry on cavitation in Herschel Venturi-tubes applied to liquid flow metering*. ISFFM, Conference Paper, Arlington.

CHARIÈRRE B., DECAIX J., GONCALVES E. 2015. *A comparative study of cavitation models in a Venturi flow*. Europan Journal of Mechanics B/Fluids, 49: 287–297.

DECAIX J., GONCALVES E. 2013. *Investigations of a three-dimensional effects on a cavitating Venturi flow*. International Heat and Fluid Flow, 53: 40–48.

GHASSEMI H., FASIH H.F. 2011. *Application of small size cavitating Venturi as flow controller and flow meter*. Flow Measurement and Instrumentation, 22: 406–412.

HUNSAKER J.C. 1935. *Progress report on cavitation research at MIT*. ASME Transactions, 57(7): 423–424.

KNAPP R.T., DAILY J.W., HAMMIT F.G. 1970. *Cavitation*. McGraw-Hill, New York.

NOSKIEVIČ J. 1969. *Kavitace*. Akademia, Praha.

NUMACHI F., KOBAYASCHI R. 1964. *Einflus der Kavitation auf die Durchfluszahl der Venturiduse*. Forsch. Ing.-Wes., 30(3): 86–93.

NUMACHI F., KOBAYASCHI R., KAMIYAMA S. 1962. *Effect of cavitation on the accuracy of Herschel-type Venturi tubes*. Trans. ASME, Series D. J. Basic Engng., 84(3): 351–362.

PALAU-SALVADOR G., GONZÁLEZ-ALTOZANO P., ARVIZA VALVERDE J. 2007. *Numerical modeling of cavitating flows for simple geometries using FLUENT V6.1*. Spanish Journal of Agricultural Research, 5(4): 460–469.

RANDALL L.N. 1952. *Rocket applications of the cavitating Venturi*. J Am Rock Soc. 22: 28–38.

REYNOLDS O. 1894. *Experiments showing the boiling of water in an open tube at ordinary temperatures*. Scientific Papers on Mechanical and Physical Subject. II. Cambridge University Press, Cambridge, 1900–1903: 578–587.

RODIO M.G., CONGEDO P.M. 2014. *Robust analysis of cavitating flow in Venturi tube*. Europan Journal of Mechanics B/Fluids, 44: 88–99.

SOBIESKI W. 2013. *Relationships between CFD and experimental fluid mechanic*. Technical Sciences, 16(3): 169–177.

SOBIESKI W. 2004. *Stanowisko laboratoryjne do badania zjawiska kawitacji metodą wibroakustyczną*. Diagnostyka, 32: 37–42.

SOBIESKI W. 2005. *Stanowisko laboratoryjne do badania zjawiska kawitacji*. V Warsztaty „Modelowanie przepływów wielofazowych w układach termochemicznych. Zaawansowane techniki pomiarowe", Stawiska.

TAMHANKAR N., PANDHARE A., JOGLEKAR J., BANSODE V. 2014. *Experimental and CFD analysis of flow through venturimeter to determine the coefficient of discharge*. International Journal of Latest Trends in Engineering and Technology, 3(4): 194–200.

Technical Sciences, 2016, 19(2) 165–187

Quarterly peer-reviewed scientific journal
ISSN 1505-4675
e-ISSN 2083-4527
TECHNICAL SCIENCES
Homepage: www.uwm.edu.pl/techsci/

A NEW APPROACH FOR OBTAINING THE GEOMETRIC PROPERTIES OF A GRANULAR POROUS BED BASED ON DEM SIMULATIONS

Wojciech Sobieski, Waldemar Dudda, Seweryn Lipiński

Department of Mechanics and Basics of Machine Construction
University of Warmia and Mazury in Olsztyn

Received 17 July 2015, accepted 23 February 2016, available online 13 June 2016

Key words: granular beds, spatial structure, Discrete Element Method, PathFinder code.

Abstract

In the article, a new way for obtaining a set of geometrical parameters of granular porous beds is presented, if the data on the locations and sizes of all particles is available. The input data were prepared with the use of Discrete Element Method. The other way for acquiring the input data may be the application of Computed Tomography (CT) and Image Analysis (IA) techniques. All geometrical parameters are calculated with the use of own numerical code called PathFinder (freely available in the Internet together with its source code). In addition to description of the method of calculations, two examples of its use are presented. One simulation was performed in PFC^{3D} code, and the other in YADE software. The aim of the article was to show clearly that a porosity is not sufficient to describe the spatial structure of a porous body. In both presented examples, the porosity value is almost the same, but other parameters, e.g. tortuosity, are different. The motivation to write the PathFinder code were significant problems with obtaining geometrical parameters needed in investigations related to granular porous media. The issues described in the article are a part of an overall research methodology relating to the linking the micro- and macro-scale investigations of granular porous beds. The areas of applications of this methodology are not discussed in the article.

Introduction

In the investigations of fluid flows through porous media, two basic concepts can be distinguished. In the first approach, the porous medium is treated as a matter, which causes flow resistance, and, in a consequence, the

Correspondence: Wojciech Sobieski, Katedra Mechaniki i Podstaw Konstrukcji Maszyn, Uniwersytet Warmińsko-Mazurski, ul. M. Oczapowskiego 11, 10-957 Olsztyn, phone: +48 89 523 32 40, e-mail: wojciech.sobieski@uwm.edu.pl.

pressure drop along the flow direction. In the simplest variant of this approach, it is not important, what is the source of the flow resistance – the global effect is what counts. This is the oldest way for describing or predicting the pressure drop in real flow systems. The Darcy law (DARCY 1856) was the first law in this field and is still one of the most important laws in the porous media research area. In the following years other laws were formulated, like for example the Forchheimer law (1901) (WHITAKER 1996), which expand the range of flows that are possible to be modelled, but the idea was the same all the time. More information about Darcy and Forchheimer laws, as well as the discussion of ranges of their application, can be found for example in the article (SOBIESKI, TRYKOZKO 2011). The main disadvantage of the first approach is the difficulty of connecting the general macro-scale effect (the pressure drop) with the phenomena taking place in the micro-scale (the energy losses due to the friction). Many mathematical models can be found in publications, where such interactions between both scales are sought. The Kozeny-Carman law (KOZENY 1927, CARMAN 1997), Ergun law (ERGUN 1952), Ergun-Wu law (WU et al. 2008), Comiti (COMITI, RENAUD 1989), Barree-Conway law (WU et al. 2011, ZHANG 2013) and other laws can be used as examples. The probability theory and fractal theory are quite popular too. These investigations show the main tendency: from macro-scale to micro-scale.

The second approach is focusing on the physical side of the problem. Here the physical phenomena occurring in the channels inside porous media are most important. The friction (and hence the geometry of these channels) plays the key role in the discussed approach. The importance of this approach increased significantly when the methods of Computational Fluid Dynamic (CFD) became widely available. Thus, the full Navier-Stokes or Reynolds equations may be used for predicting the fluid behaviour in porous zone for many kinds of porous media. Currently, many researchers are trying to understand the processes on micro-scale and their impact on the behaviour in macro-scale. In this approach, the research path leads from micro-scale to macro-scale.

In the current article a new look on the problem in context of granular porous beds (porous media consisting of spherical or quasi-spherical particles) is proposed. In this approach, the research methodology includes three main stages (Fig. 1):

– Acquiring in micro-scale information about the size and location of each particle forming a porous bed.

– Basing on these data, calculating the porosity, tortuosity, specific surface of the porous body and other parameters that can macroscopically characterize the pore space of this type of media.

– Calculating the linear and non-linear terms of macro-scale laws (e.g. Kozeny-Carman law), basing on the structure analyzed at the micro level.

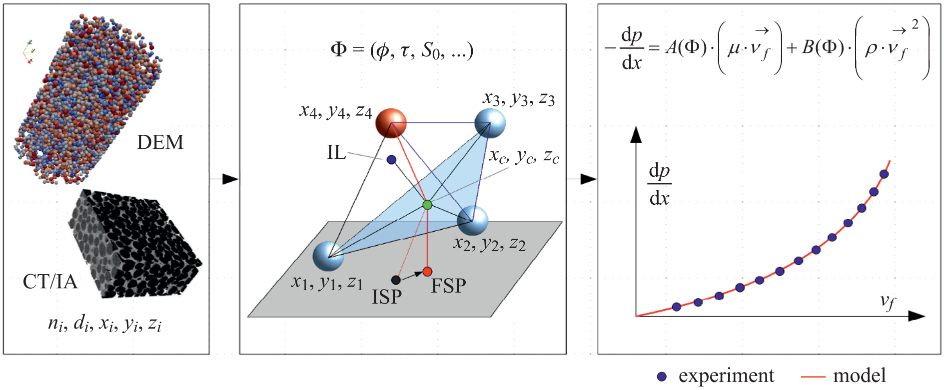

Fig. 1. Schematic representation of the overall research methodology

The realization of the first stage is possible in two ways. The first way is to carry out computer simulations using Discrete Element Method (DEM). In this method all needed data can be obtained directly, through a proper record of the results of the calculations in files. This very method is used in hereby article. The second way is the use of Computed Tomography and the Image Analysis. In this method all needed data can be achieved by appropriate algorithms of image processing which allows to transform a series of CT images into knowledge about the spatial structure of the porous bed.

To calculate a set of geometrical parameters characterizing the spatial structure of porous beds, new algorithms were needed. They were developed first (details in the research report, SOBIESKI 2009a) and then the PathFinder code (*The PathFinder Project*. Online) was written. The current article presents mainly this part of the proposed research methodology.

Having established the information about the spatial structure of the porous bed, the third stage may be started with the creation of a macro-scale model. In the applied methodology the general Forchheimer law is used, but there may be used any different law. This law was implemented to the ANSYS Fluent CFD code by using the so-called Porous Media Model (Fluent Inc.: Fluent 6.3 User's Guide, Chapter 7.19: Porous Media Conditions, September 2006, Fluent Inc.: Fluent 6.3 Tutorial Guide. September 2006, SOBIESKI 2010) and the User Defined Functions (UDF). In this way a full control of the model is provided and all spatial parameters may be introduced as constant values or functions dependent on the location or time.

The general set of input data for macro-scale laws

Many laws for calculating the pressure drop in fluid flow systems with porous media can be shown in a unified form (Sobieski, Trykozko 2011, 2014a, b):

$$\frac{\mathrm{d}p}{\mathrm{d}x} = A(\Phi) \cdot (\mu \cdot \vec{v}_f) + B(\Phi) \cdot (\rho \cdot \vec{v}_f) \tag{1}$$

where:
p – pressure [Pa],
x – a coordinate along which the pressure drop occurs [m],
$A(\Phi)$ and $B(\Phi)$ – two generalized parameters, dependent on the set Φ characterizing the spatial structure of the porous medium,
μ – dynamic viscosity of the fluid [kg/m · s)],
ρ – density of the fluid [kg/m^3)],
$\vec{v}_f$ – filtration velocity [m/s].

The commonly used Kozeny-Carman equation may serve as an example of a law with the structure like the one in formula (1). This equation is derived for calculating the permeability of well-sorted sand (Neethirajan et al. 2006, Fourie et al. 2007), in which coefficients $A(\Phi)$ and $B(\Phi)$ have the following forms:

$$\begin{cases} A(\Phi) = \dfrac{1}{\kappa} = C_{\mathrm{KC}} \cdot \tau_f \cdot S_0 \cdot \dfrac{(1-\phi)^2}{\phi^3} \\ B(\Phi) = 0 \end{cases} \tag{2}$$

where:
κ – permeability [m^2],
C_{KC} – Kozeny-Carman pore shape factor (a model constant), which should be equal to 5.0 (Carman 1997) [–],
τ_f – the tortuosity factor [m^2/m^2] defined as the square of the tortuosity τ [m/m],
S_0 – specific surface of the porous body [1/m],
ϕ – porosity [m^3/m^3].

It should be noted that researchers have also used other forms of Kozeny-Carman equation (Dunn 1999, Rainey et al. 2008, Resch 2008, Rossel 2004). A larger discussion on this topic was presented in the work (Sobieski 2014).

Another known law, matching formula (1), is the Ergun equation (Ergun 1952, Niven 2002, Hernández 2005, Dunn 1999), in which:

$$\begin{cases} A(\Phi) = 150 \cdot \dfrac{(1-\phi)^2}{\phi^3 \cdot (\psi \cdot d)^2} \\ \\ B(\Phi) = 1.75 \cdot \dfrac{(1-\phi)}{\phi^3 \cdot (\psi \cdot d)} \end{cases} \tag{3}$$

where:

d – the representative (e.g. average) diameter of particles forming a porous bed [m],

ψ – sphericity coefficient [–] (less than 1 in general and equal to 1 when the particles are spherical in shape, Sobieski 2009b).

In the literature one can find many other formulas for $A(\Phi)$ and $B(\Phi)$ coefficients (e.g., Mian (1992), Skjente et al. (1999), Samsuri et al. (2000), Belyadi a (2006), Belyadi (2006), Lord et al. (2006), Amao (2007), Wu and Yu (Wu et al. 2007), but almost all of them are related to the geometrical structure of the porous media.

The mathematical forms of physical laws cited here are not very important in this article and they serve only as examples. The most important is the fact, that usually only a few basic geometrical parameters are needed for modelling the fluid flows through porous beds. Such set may be also defined as follows:

$$\Phi = \{d, \phi(V_p,V),\ \varepsilon(V_s,V),\ \tau(L_p,L_0),\ S_0(S_s,V_s,V),\ \psi(l_x,l_y,l_z)...\} \tag{4}$$

where:

V_p – the total volume of the pore part of a porous medium (filled by a fluid) [m^3],

V_s – the total volume of all particles in the bed [m^3],

V – the total volume of a porous medium [m^3],

L_p – the length of a flow path [m],

L_0 – the depth of the porous medium in the main flow direction [m],

S_s – the total inner surface of a solid body [m^2],

l_x,l_y,l_z – the particle size in three directions of the space [m].

Having established the parameters of set Φ, both $A(\Phi)$ and $B(\Phi)$ terms may be calculated, according to the formulas (2), (3) or others. Of course, the parameters set can be used for other purposes.

It is worth noting, that some parameters of the Φ set can be obtained very easily (assuming that the data with locations and sizes of all particles is available). Others, in turn, are very difficult to determine. It would be advantageous to have a convenient tool that allows obtaining all the information. The PathFinder numerical code is created to be such a tool. In the work (SOBIESKI et al. 2012) the method of tortuosity calculation was shown. In the current article, a newly developed version of this algorithm is described as well as other parts of the whole calculation algorithm implemented into the PathFinder code. In authors' opinion, this new numerical code may be very useful for the researchers dealing with granular porous media – especially, that the PathFinder software is freely available in the Internet together with the source code (*The PathFinger Project*. Online).

The calculation methods

The PathFinder code

The PathFinder software is intended for calculating a set of geometrical parameters of a porous bed, when the data with locations and sizes of all particles is available. PathFinder in fact is only a solver and the visualization should be made in Gnuplot environment (Gnuplot Home Page. Online) (during calculations) or in ParaView software (ParaView Home Page. Online) (after calculations). PathFinder automatically generates suitable output files for that purpose, in a form of a simple text, in VTK or CSV formats, as well as shell scripts for an operating system. Using other, additional applications for the results visualization is possible, too (e.g. The MayaVi Data Visualizer. Online).

The PathFinder software works with a text file with five columns which contain information in the following order: consecutive numbers of each sphere, X, Y and Z-coordinates of centres of spheres and diameters of spheres. The X and Y columns may be swapped, but the Z column must be always the fourth. This is important because it is assumed that this is the main flow direction. In data reading process, every line is considered as a new particle, so the number of lines gives information about the bed size.

For PathFinder it is not relevant in which way the input file was generated: using either results of the Discrete Element Method (DEM) simulation or the results of Computed Tomography and the 3D Image Analysis. In the present article two examples from the first variant are used (Fig. 2). The left figure presents a cylindrical domain with 18188 particles (DEM simulation was made in PFC^{3D} code, ITASCATM Home Page. Online) and the right a cuboid domain

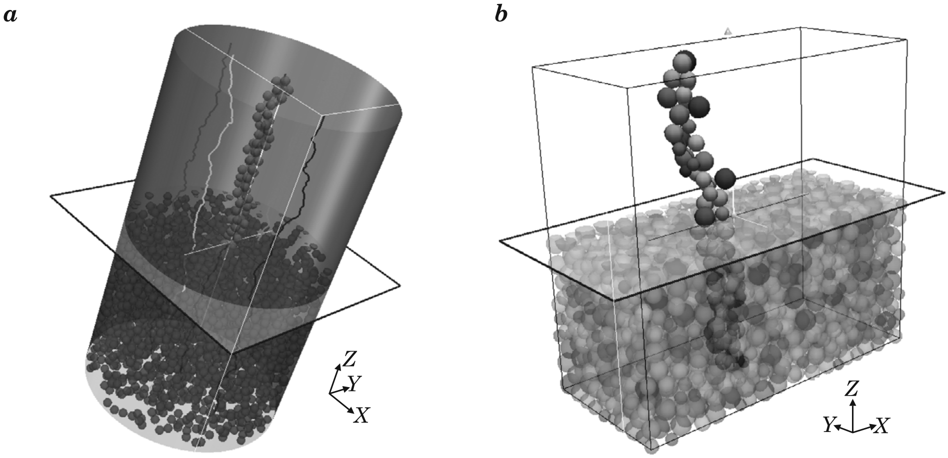

Fig. 2. Examples of visualisation the results obtained in the FathFinder code

with 4000 particles (DEM simulation was made in YADE code, YADE Home Page. Online). In both examples, a central path with surrounding particles is shown.

Calculating the domain range

Under the expression „calculation domain", a virtual space is meant here, where all calculations take place. Usually the domain volume is the same as the bed volume.

All spheres in the bed are described by 5 variables: n_i – number of the i-th sphere; x_i – X coordinate of the i-th sphere centre; y_i – Y coordinate of the i-th sphere centre; z_i – Z coordinate of the i-th sphere centre; d_i – diameter of the i-th sphere. The total number of spheres in the bed is denoted by n_s.

In the first step, all spheres are sorted by the Z coordinate. In this way, the sphere lying lowest in the bed has the index $i = 1$ and the highest sphere index is $i = n_s$. In determination of the Z-axis range, the particle diameters are taken into account (Fig. 3):

$$z_{\min} = \min\left(z_i - \frac{1}{2}\cdot d_i\right),\ z_{\max} = \max\left(z_i + \frac{1}{2}\cdot d_i\right) \tag{5}$$

Note, that if the bottom surface of the bed is horizontal and flat, many particles have the lowest surface point in the same XY plane. In the same way the ranges of X and Y axis are calculated.

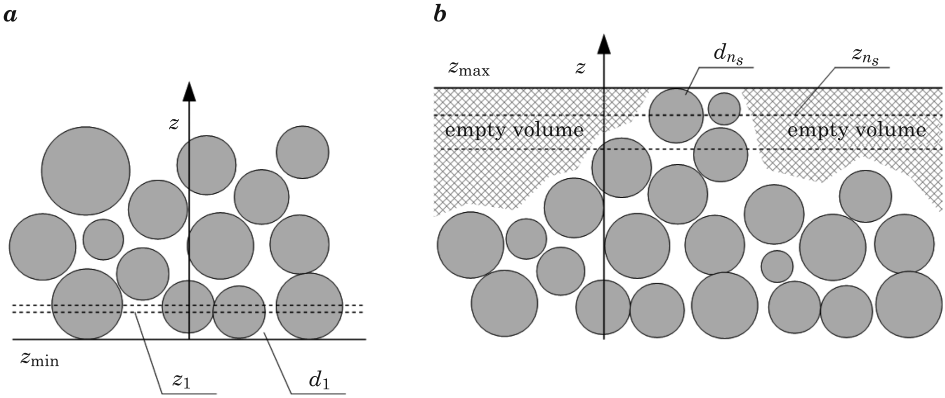

Fig. 3. Calculating the location of the bottom and top surface of the bed

In real beds, the bottom and the lateral surfaces usually limit the locations of particles. However, the top surface can be uneven and some particles may protrude from the bed. In this case, „empty volume" in the bed exists, what may give inaccuracies in calculations. To avoid this, all protruding particles should be rejected from the calculations (Fig. 4). As a result, the volume of the calculation domain is a little less than the real bed volume. The number of rejected particles is described by variable n_{s_rej}. Also, notice the small particle right to the particle determining the height of the bed (before discarding protruding particles). Despite the fact that it has the highest value of Z coordinate, it is not recognized by the algorithm as the highest sphere in the bed due to its small diameter.

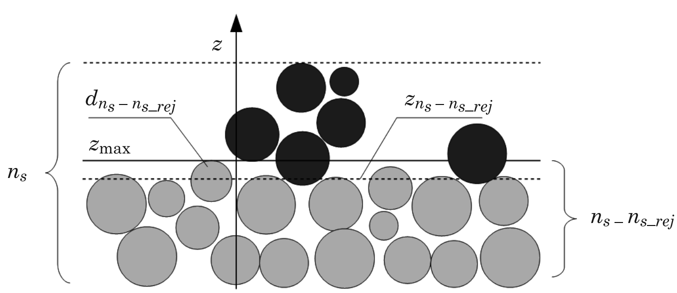

Fig. 4. Visualization of the idea of rejecting protrudes particles: the empty volume is not taken into account

Calculating the default Initial Starting Point

The default Initial Starting Point (ISP), from which the algorithm starts, is calculated as

$$x_0 = x_{\min} + \frac{x_{\max} - x_{\min}}{2},\ y_0 = y_{\min} + \frac{y_{\max} - y_{\min}}{2},\ z_0 = z_{\min} \tag{6}$$

where index 0 denotes the ISP. In the PathFinder source code, the same variables are then used for the Final Starting Point (FSP).

Calculating the domain height

The domain height is calculated as

$$L_0 = z_{n_s - n_{s\_rej}} + 0.5 \cdot d_{n_s - n_{s\_rej}} - z_{\min} \tag{7}$$

where:
L_0 – the height of the calculation domain [m],
$z_{n_s - n_{s\_rej}}$ – the Z coordinate of the highest used in calculations sphere in the bed [m],
$0.5 \cdot d_{n_s - n_{s\_rej}}$ – the radius of the highest used in calculations sphere in the bed [m].

Calculating the domain volume

In the PathFinder code, calculations can be performed in porous beds (domains) in cuboid and cylindrical shapes. In the cases when the source geometry is complex (in DEM models or when the objects are scanned with the use of the CT technique), a representative part of the porous bed with an appropriate shape must be exported for the PathFinder needs.

In the case of a cuboid shape the volume of the domain is calculated from the following formula:

$$V = (x_{\max} - x_{\min}) \cdot (y_{\max} - y_{\min}) \cdot L_0 \tag{8}$$

When the porous bed has a cylindrical shape, the domain volume is calculated as follows:

$$V = \frac{\pi \cdot d_{cyl}^2}{4} \cdot L_0 \tag{9}$$

where:
d_{cyl} is the diameter of the cylinder [m],

calculated as the average range of X and Y axis:

$$d_{cyl} = \frac{1}{2}\left[(x_{\max} - x_{\min}) \cdot (y_{\max} - y_{\min})\right] \tag{10}$$

Calculating the tortuosity

Tortuosity is the ratio of the actual length of flow path to the physical depth of a porous bed:

$$\tau = \frac{L_p}{L_0} \tag{11}$$

where:
τ – the tortuosity [m/m],
L_p – the length of a flow path [m].

Note, that the tortuosity may be interpreted as a geometrical parameter: the length of a typical pore channel (which is independent of the filtration velocity) or as a flow parameter: the length of a typical fluid stream (which is dependent on the filtration velocity). In the PathFinder code only the geometrical tortuosity may be directly calculated.

The algorithm (so-called Path Tracking Method) for calculating length L_p in PathFinder was described in details in the papers SOBIESKI (2009a), SOBIESKI et al. (2012) and DUDDA, SOBIESKI (2014). Here is the summarized procedure (Fig. 5; particles are not in a scale):

– Arbitrarily choose an Initial Starting Point (ISP) at the bottom of the porous bed (*a*);

– Find three nearest particles to the ISP that form a triangle in the space (*b*);

– Calculate the coordinates of the centre of gravity of the surface (in the triangle plane) through which flows the fluid (this part was changed since the work SOBIESKI et al. 2012 was published) (*c*);

– Move the ISP to the Final Starting Point (FSP) – in this way the first path section is perpendicular to the bottom surface of the bed (*d*);

– Calculate the normal to the triangle, in the direction of Z axis;

– Estimate coordinates of the so-called Ideal Location (IL), in which the next sphere surrounding the path should be located (*e*);

– Move the IL closer to the triangle centre (*f*);

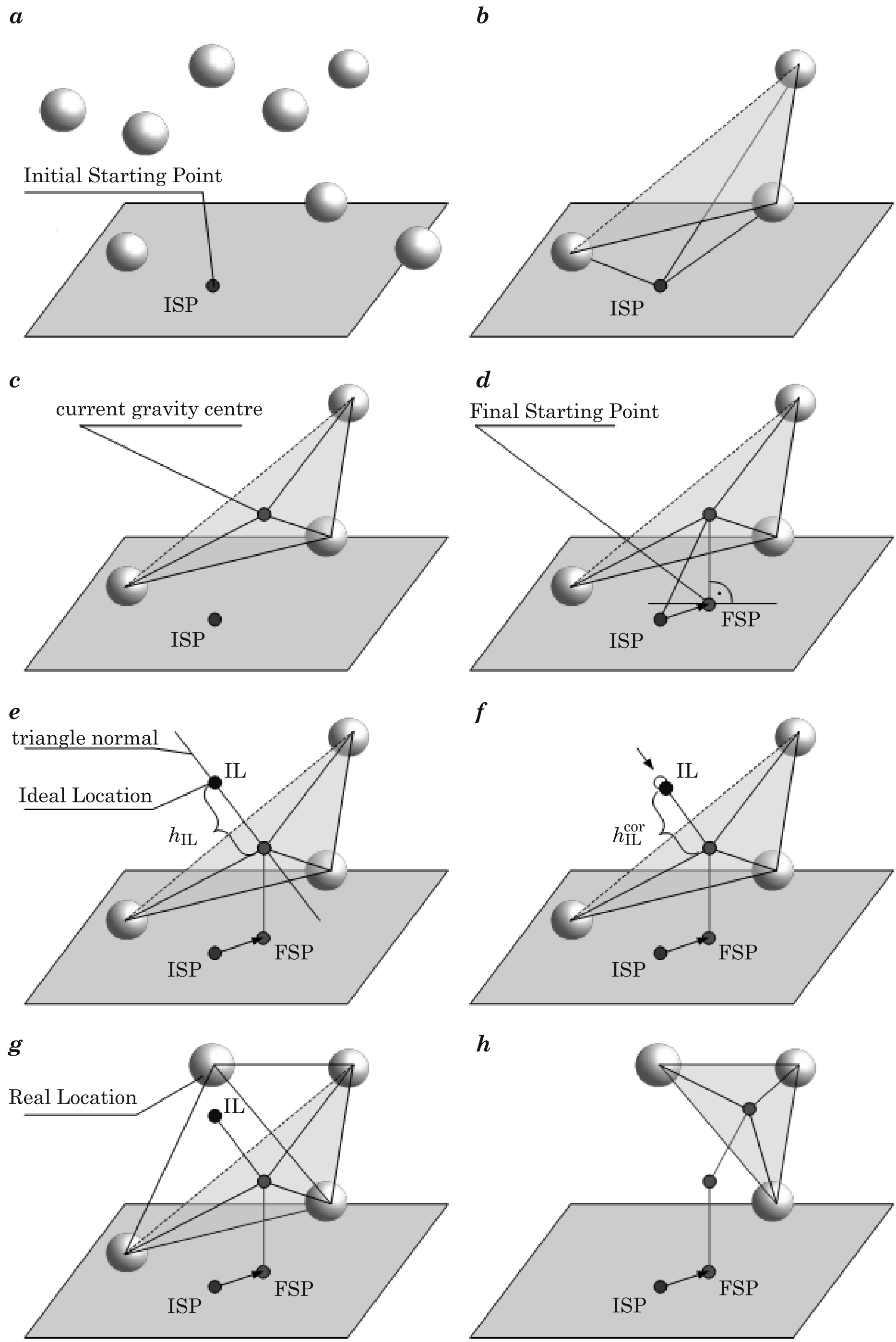

Fig. 5. Scheme of the main steps in the tortuosity algorithm; description in the text

– Find the nearest particle to the IL – this is the Real Location (RL) of the 4-th particle forming tetrahedron in the space (*g*);

– Remove the lowest sphere from tetrahedron 1-2-3-4 to obtain the base triangle for the next tetrahedron (*h*);

– Continue the calculations from the third point until reaching the top surface of the bed;

– Calculate the length of the path inside the tetrahedron (a flow path is a line connecting the centroid of the base triangle with the centroid of one of the three side triangles).

The algorithm finishes when the distance between current IL and the nearest particle centre is bigger than the distance between the top surface of the bed and the Z coordinate of the IL. The last section is perpendicular to the top surface of the bed.

The number of path points is higher by two in relation to the number of tetrahedrons used for searching the path sections.

In the PathFinder code an additional algorithm allows to smooth the path exists. Due to this, the path length is a little shorter. The use of the smoothed value is currently not recommended.

Calculation of the triangle centre of gravity

The algorithm for calculating the centre of gravity of the shape, through which the fluid flows, is described in details in the work DUDDA and SOBIESKI (2014). This algorithm consists of two stages. First, the coordinates of all basic figures are calculated (one triangle and three circle segments) and next, the summation method is used to calculate coordinates of the resultant centre of gravity of the set of basic shapes (Fig. 6)

$$
\begin{aligned}
x_{gc} &= \frac{A_t \cdot x_{tc} - A_1 \cdot x_{s1} - A_2 \cdot x_{s2} - A_3 \cdot x_{s3}}{A_t - A_1 - A_2 - A_3} \\
y_{gc} &= \frac{A_t \cdot y_{tc} - A_1 \cdot y_{s1} - A_2 \cdot y_{s2} - A_3 \cdot x_{s3}}{A_t - A_1 - A_2 - A_3} \\
z_{gc} &= \frac{A_t \cdot z_{tc} - A_1 \cdot z_{s1} - A_2 \cdot z_{s2} - A_3 \cdot z_{s3}}{A_t - A_1 - A_2 - A_3}
\end{aligned}
\tag{12}
$$

where:

x_{gc}, y_{gc}, z_{gc} – coordinates of the obtained centre of gravity [m],

A_t – the area of the current triangle [m^2],

x_{tc}, y_{tc}, z_{tc} – coordinates of the current triangle centre [m],
$A_{1,2,3}$ – areas of circle segments [m2],
x_s, y_s, z_s – coordinates of gravity centres (denoted by the sign) of circle segments [m].

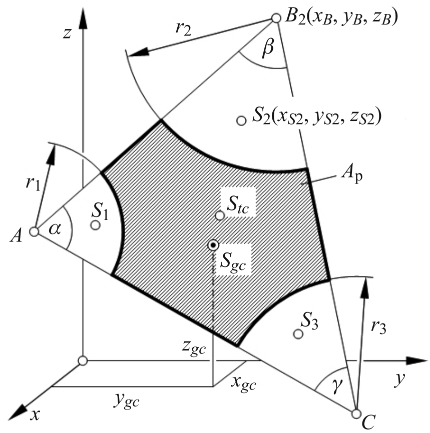

Fig. 6. The shape, through which the fluid flows and its gravity centre

The Ideal Location and its correction

For calculating the Ideal Location, a characteristic dimension is used. It can be the average length of the current triangle sides l_{ave} (recommended) or the average diameter of spheres d_{ave} forming the current triangle. In consecutive calculations it was assumed, that the tetrahedron is regular and all sides have lengths equal to the characteristic dimension. In that case, the height of such tetrahedron may be calculated from the simple formula:

$$h_{IL} = c_{dim} \cdot \sqrt{\frac{2}{3}} \tag{13}$$

where:
h_{IL} – the predicted distance between the IL and the triangle plane [m],
c_{dim} – the characteristic dimension [m].

Height h_{IL} is measured on the triangle normal in the direction of increasing values of the Z coordinate.

In real systems, particles forming a triangle may not touch one another, which results is that the fourth particle falling partly between them. In extreme cases, the fourth particle can slide completely between particles that form the triangle. That can happen when the actual triangle area is three times larger than the area of a triangle with one side equal to the average diameter of the spheres forming the current triangle (derived in SOBIESKI 2009a). If this ratio is higher than 3, a correction algorithm is used (it may be turned off using the settings file) and new three particles close to the current triangle centre are then searched. The number of such corrected triangles is shown in the final report. This normalized critical area of the triangle is also included in the settings file, but impossible to omit entirely.

Usually the area of the real triangle is far from the critical area and the „sinking" effect is small, but not to omit. Therefore, the formula (13) should rather be defined as follows:

$$h_{\mathrm{IL}} = c_{\mathrm{dim}} \cdot h_{\mathrm{cor}} \sqrt{\frac{2}{3}} \tag{14}$$

where:
h_{cor} is a correction coefficient for the Ideal Location [–].

This coefficient may be defined (in the settings file) as a constant value:

$$h_{\mathrm{cor}} = 0.5 \tag{15}$$

or a function:

$$h_{\mathrm{cor}} = f(\mathrm{I_A}) = 1 - \frac{\exp(a \cdot (I_A - b))}{1 + \exp(a \cdot (I_A - b))} \tag{16}$$

where:
I_A – the area indicator [–],
a – a coefficient (obtained in earlier numerical investigations SOBIESKI 2009a) responsible for the function gradient and equal to 8.0 [–],
b – a coefficient (obtained in earlier numerical investigations SOBIESKI 2009a) equal to average value of normalized triangle area for the whole porous bed, with value equal to 0.5 [–].

The area indicator is defied as

$$I_A = \frac{A_i}{A_0} \tag{17}$$

where the current triangle area is calculated from the Heron formula

$$A_i = \sqrt{\frac{L}{2} \cdot \left(\frac{L}{2} - a\right) \cdot \left(\frac{L}{2} - b\right) \left(\frac{L}{2} - c\right)} \tag{18}$$

and the area of the reference triangle A_0 (triangle with all sides equal to the characteristic dimension) as

$$A_0 = \frac{c_{\mathrm{dim}} \cdot \sqrt{3}}{4} \tag{19}$$

Symbols a, b and c in formula (18) denotes lengths of current triangle sides [m].

The details about this issue as well as the way of obtaining all constants are described in a research report (SOBIESKI 2009a), which was written parallel to performing implementation actions. This report contains descriptions of many issues not mentioned in the hereby article and shows the process of creation the final version of the Path Tracking Method.

Calculating the porosity

Having obtained the information about diameters of all particles in the bed, the total volume of all particles in the porous bed can be calculated. This can be done as follows:

$$V_s = \sum_{i=1}^{n_s - n_{s\_rej}} \frac{\pi \cdot d_i^3}{6} \tag{20}$$

where:
V_s – the total volume of all particles in the bed [m^3],
d_i – the diameter of the i-th particle in the bed [m].

Using the formula (8) or (9) and the equation (20), the porosity of the granular bed may be consequently calculated as:

$$\phi = \frac{V_p}{V} = \frac{V - V_s}{V} = 1 - \frac{V_s}{V} \tag{21}$$

Calculating the inner and the specific surface of the solid body

The inner surface of the solid body may be obtained from the following formula (assuming point contacts between particles)

$$S_p = S_s = \sum_{i=1}^{n_s - n_{s\_rej}} \pi \cdot d_i^2 \tag{22}$$

where:
S_p – the total surface of the pore space in the bed [m^2],
S_s – the total surface of all particles in the bed [m^2].

The specific surface of the porous body is calculated in two ways, i.e. according to the Kozeny theory (KOZENY 1927):

$$S_{0,\mathrm{Kozeny}} = \frac{S_p}{V} \tag{23}$$

and to the Carman theory (CARMAN 1997):

$$S_{0,\mathrm{Carman}} = \frac{S_p}{V_s} \tag{24}$$

The relationship between both definitions is as follows:

$$\frac{S_{0,\mathrm{Kozeny}}}{S_{0,\mathrm{Carman}}} = 1 - \phi \tag{25}$$

The approach to the definition of the specific surface of the porous body is one of the differences between the Kozeny equation and the Carman formula.

Calculation examples

In Table 1 there are settings of PathFinder calculations for the two examples previously described. All calculations were made with use of version IV.1 of the PathFinder code.

Table 1

Settings for the calculations in the PathFinder code

Settings	Units	YADE	PFC^{3D}
Number of particles	[–]	4000	18188
Particle diameter	[mm]	31.1 – 57.7	5.5 – 7.5
Domain geometry	[–]	cuboids	cylinder
ISP location	[–]	00	00
ISP x shift	[–]	0.5	0.5
ISP y shift	[–]	0.5	–
Number of rejected particles	[–]	0	19
Triangle center calculating method	[–]	gravity centre	gravity centre
Characteristic dimension	[–]	l_{ave}	l_{ave}
Correction method for the IL	[–]	function	function
Correction coef. for constant method	[–]	0.5	0.5
a parameter for function method	[–]	0.8	0.8
b parameter for function method	[–]	1.3	1.3
Critical area triangle correction	[–]	Yes	Yes
Critical area of the triangle	[–]	3.0	3.0
Smooth the path	[–]	No	No

The number of rejected particles n_{s_rej} for performing coarse calculations should be set to zero. If there is a suspicion of a free space existence (like in the case shown in Fig. 3), this value should be increased. The best way to obtain this parameter is to perform a set of calculations with different n_{s_rej} values and to observe results, particularly the porosity value. A relationship between the number of rejected particles and the porosity value may be prepared here (e.g. in a graphical form). On this basis, the best value of this parameter can be chosen. This method was used for obtaining this parameter for the PFC^{3D} example (SOBIESKI 2009a), in which a free surface of the porous bed exists. In the example from YADE, the number of rejected particles equal zero, due to the way of DEM modelling. All walls were set as flat surfaces, moving closer to each other during calculations. In such a case, no empty area exists in the modelled system. In the PathFinder software, the ISP must be chosen for performing the calculations. The simplest way is to choose ISP directly in the settings file as one from 9 default locations (SOBIESKI 2009a, SOBIESKI et al. 2012, SOBIESKI, LIPIŃSKI online). The description of point location contains two signs (Fig. 7): the first concerns the X axis, the second the Y axis. Both signs may have values: „–” (the negative part of the axis), „0” (zero point of the axis) and „+” (the positive part of the axis). The combination of signs is as follows: +0, + –, 0 –, – –, –0, – +, 0+, ++, 00.

By default, all points surrounding the zero point of X and Y axis are located in the middle of the section connecting the zero point and the domain wall. The distance may be changed by using options x-shift and y-shift available in the settings file. These coefficients may be set between 0 (the ISP is in the zero point – the middle of the bottom domain wall) and 1 (the ISP is on the wall). The default values for both coefficients are 0.5. This value is not important in the current point, because only one path, from the central point, is calculated.

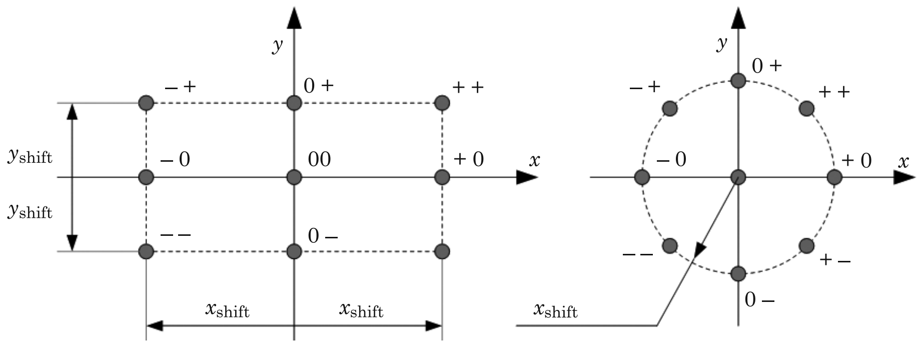

Fig. 7. Default locations of the Initial Starting Point for both possible types of domain

In both examples the recommended values for the characteristic dimension (l_{ave}), the correction method (function) and its coefficients (a and b), the critical area of the triangle, and the method for calculating the triangle centre (gravity centre) were used.

Table 2 contains the calculation results for both test examples. The numbers of path points inform how many of tetrahedral structures were found in the iteration process. In every structure of this kind, one section of the path is located. The number of tetrahedral structures is always lowered by 2. Thus

Table 2

Results of calculations

Settings	Units	YADE	PFC^{3D}
Number of path points	[–]	59	130
Number of path rejected points	[–]	0	0
Number of corrected triangles	[–]	0	0
Bed (domain) height	[m]	0.883302	0.254938
Length of the path	[m]	1.053803	0.317288
Average angle between path sections	[°]	141.557825	139.109342
Tortuosity	[m/m]	1.193026	1.244571
Volume of the bed (domain)	[m^3]	0.345158	0.004505
Inner surface of the solid body	[m^2]	25.534886	2.393343
Specific surface (Kozeny def.)	[1/m]	73.980321	531.227627
Specific surface (Carman def.)	[1/m]	127.652558	915.918417
Volume of the porous body	[m^3]	0.200034	0.002613
Porosity	[m^3/m^3]	0.420456	0.420006
Ergun A	[$1/m^2$]	343565.12	16372081.72
Ergun 2*B	[1/m]	614.39	4248.07
Kozeny-Carman term	[$1/m^2$]	524013.00	29498873.86

is due to the fact that the first (FSP) and the last path point are calculated in different way.

During the calculations, it is checked whether there are duplicate points. If yes, one of them is removed from the path and the appropriate information is shown in the final report.

The number of corrected triangles gives information of how many times the corrections based on critical area of the triangle were made (duplicate points may be created in such case). This value should be zero – other values mean that in the bed probably a structural non-continuity exists locally. Sometimes such a case does occur. The importance of other values contained in Table 2 has been already explained.

It should be added here, that the *B* term in the Ergun law is doubled in the final report. This is because this term must be introduced in this way in the ANSYS Fluent software (Fluent Inc.: Fluent 6.3 User's Guide, Chapter 7.19: Porous Media Conditions, September 2006, Fluent Inc.: Fluent 6.3 Tutorial Guide. September 2006) (but only if the interface is used, not the UDF technique).

PathFinder gives possibility to present results of calculation in a graphical form. The most important visualization may be performed using the ParaView or MayaVi software. Details about the visualisation processes are described in the PathFinder User's Guide (SOBIESKI et al. 2012). In Figure 8 there is the original porous bed created in the PFC^{3D} code (LIU et al. 2008a, b). Additionally the calculation results of the PathFinder code are visible there and these are: five paths, the spheres surrounding the paths, as well as the tetrahedral structures used to obtaining the path sections. The tetrahedron structures may be additionally coloured according to few scalars: values of triangle areas, values of flow areas, values of perimeters (of the triangle, of the flow shape, and of the friction), values of the quality indicators, values of angles between triangle normal and the *Z*-axis and others. The central path with surrounding spheres and a part of the bed for the YADE example, was shown earlier in Figure 2 (right).

The other way of visualization calculation results is using scripts of the Gnuplot graphical environment. Thanks to them, one can follow the process of calculation. If appropriate option is set in the settings file, the current results may be shown in every iteration (Fig. 9): the Initial Starting Point, the Final Starting Point, the current tetrahedron, the current Ideal Location, the current Real Location, the current triangle and the next triangle. At the end, the current path may be shown. When using the Gnuplot scripts, values of all important variables may be seen, i.e. those being calculated for every tetrahedral structure. Many other Gnuplot scripts are created during such a calculation; most of them are not described here.

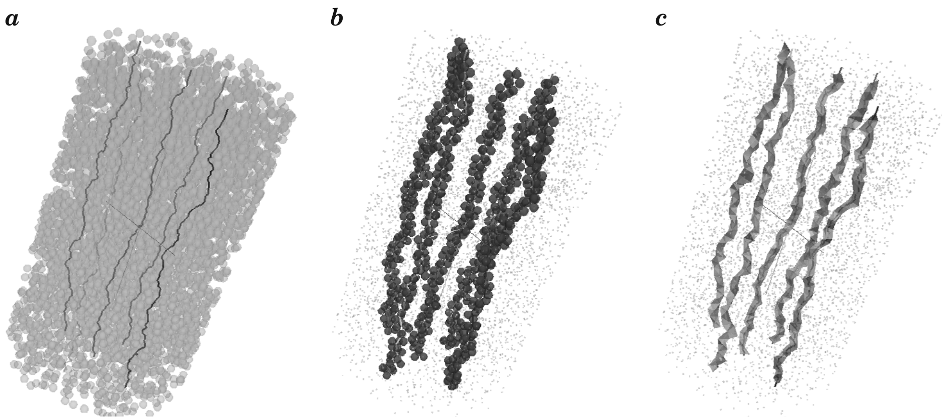

Fig. 8. Main forms of visualization of the PathFinder results (PFC[3D] example)

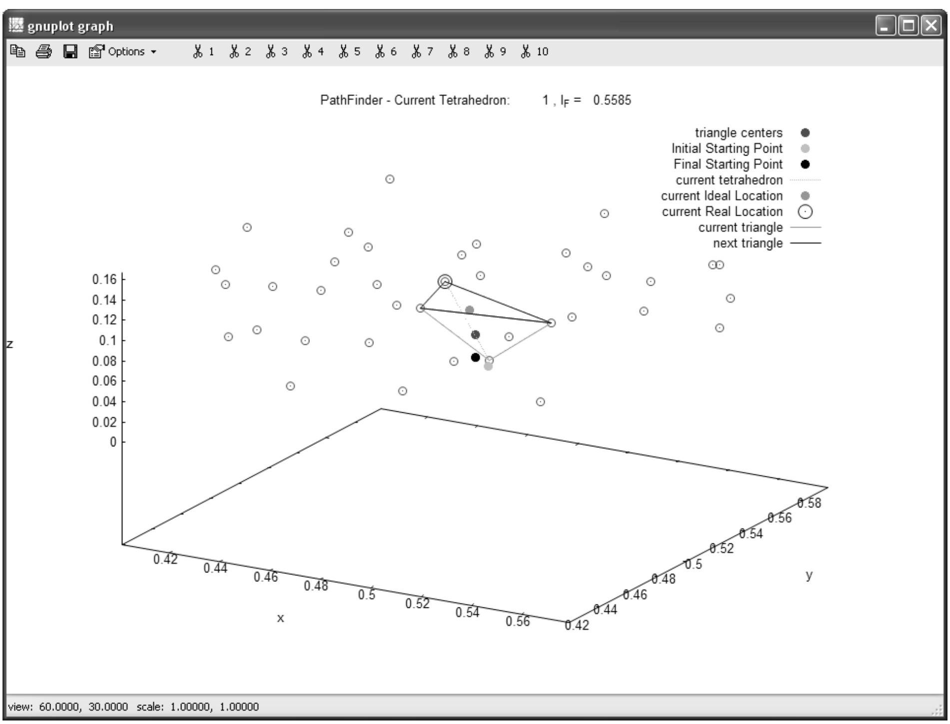

Fig. 9. Visualization of the first tetrahedron in the path (YADE example)

In the current example, only one path for every case is presented (from ISP = 00) due to the desire to show details of a calculation – some results, like the number of path rejected points (duplicates) or the number of corrected triangles must not be averaged. Nevertheless, in general the PathFinder has appropriate algorithms for automatic calculation of many paths and for comparing or averaging data. For comparison, the average tortuosity calculated for 25 paths (with x-shift and y-shift equal to 0.25, 0.5 and 0.75) is equal to 1.24 for the PFC^{3D} example, and 1.23 for the YADE example. In general it is recommended to calculate more than one path (minimum 5, SOBIESKI 2009a) and use the average value for further calculations.

Summary

The performed works can be summarized as follows:

– The porosity is not a sufficient parameter for describing the spatial structure of a porous bed. In both examples the porosity values were almost the same while other properties were different (e.g. the tortuosity).

– A relationship between tortuosity value and the average angle between path sections can be seen. When this angle is smaller, the tortuosity is higher.

– The tortuosity in the PFC^{3D} example is higher than in the second case, which is caused by the differences in the particle sizes and the diameter distribution. In consequence, the shapes of channels must be more complicated. It can be concluded that the tortuosity value depends on the diameters distribution in the bed.

– The A and B terms are different in both cases. It may stem from the fact that smaller diameters results in turn thinner pore channels. If the pore channel is thinner, the greater is the flow resistance (due to the viscosity).

– The results of calculations described in the article should be compared with other methods: analytical (e.g. porosity-tortuosity correlations available in the literature), numerical (e.g. by the use of the Lattice Boltzmann Methods or the Immersed Boundary Method) and of course experimental. Such investigations are in progress and we will publish their results in the near future.

References

AMAO A.M. 2007. *Mathematical Model For Darcy Forchheimer Flow With Applications To Well Performance Analysis*. MSc Thesis. Department of Petroleum Engineering, Texas Tech University, Lubbock, Texas.

BELYADI A. 2006. *Analysis of Single-Point Test To Determine Skin Factor*. PhD Thesis. Department of Petroleum and Natural Gas Engineering, West Virginia University, Morgantown, West Virginia.

BELYADI F. 2006. *Determining Low Permeability Formation Properties from Absolute Open Flow Potential*. PhD Thesis. Department of Petroleum and Natural Gas Engineering, West Virginia University, Morgantown, West Virginia.

CARMAN P.C. 1997. *Fluid Flow through a Granular Bed*. Transactions of the Institute of Chemical Engineers, Jubilee Supplement, 75: 32–48.

Comiti J., Renaud M.A. 1989. *New model for determining mean structure parameters of fixed beds from pressure drop measurements: application to beds packed with parallelepipedal particles*. Chemical Engineering Science, 44(7): 1539–1545.

Darcy H. 1856. Les *Fontaines Publiques De La Ville De Dijon*. Victor Dalmont, Paris.

Dudda W., Sobieski W. 2014. *Modification of the PathFinder algorithm for calculating granular beds with various particle size distributions*. Technical Sciences, 17(2): 135–148.

Dunn M.D. 1999. *Non-Newtonian Fluid Flow through Fabrics*. National Textile Center Annual Report: C98-P1, Philadelphia University, November.

Ergun S. 1952. *Fluid flow through packed columns*. Chemical Engineering Progress, 48(2): 89–94.

Fluent Inc.: Fluent 6.3 Tutorial Guide. September 2006.

Fluent Inc.: Fluent 6.3 User's Guide, Chapter 7.19: Porous Media Conditions, September 2006.

Fourie W., Said R., Young P., Barnes D.L. 2007. *The simulation of pore scale fluid flow with real world geometries obtained from X-ray computed tomography*. COMSOL Conference, Boston, United States, 14 March.

Gnuplot Home Page. Online: http://www.gnuplot.info/ (access: 1.05.2015).

Hernández Á.R.Á. 2005. *Combined Flow And Heat Transfer Characterization of Open Cell Aluminum Foams*. MSc Thesis. Mechanical Engineering, University Of Puerto Rico, Mayagez Campus, San Juan, Puerto Rico.

ITASCATM Home Page. Online: http://www.itascacg.com/pfc3d/ (access: 1.05.2015).

Kozeny J. 1927. *Über kapillare Leitung des Wassers im Boden*. Akademie der Wissenschaften in Wien, Sitzungsberichte, 136(2a): 271–306.

Liu Ch., Zhang Q., Chen Y. 2008. *PFC*^{3D} Simulations of lateral pressures in model bin. ASABE International Meeting, paper number 083340. Rhode Island.

Liu Ch., Zhang Q., Chen Y. 2008. *PFC*^{3D} Simulations of vibration characteristisc of bulk solids in storage bins. ASABE International Meeting, paper number 083339. Rhode Island.

Lord D.L., Rudeen D.K., Schatz J.F., Gilkey A.P., Hansen C.W. 2006. *DRSPALL: Spallings Model for the Waste Isolation Pilot Plant 2004 Recertification*. SAND2004-0730, Sandia National Laboratories, Albuquerque, New Mexico, Livermore, California.

Mian M.A. 1992. *Petroleum engineering handbook for the practicing engineer*. Pennwell Publishing, Tulsa, Oklahoma.

Neethirajan S., Karunakaran C., Jayas D.S., White N.D.G. 2006. *X-ray Computed Tomography Image Analysis to explain the Airflow Resistance Differences in Grain Bulks*. Biosystems Engineering, 94(4): 545–555.

Niven R.K. 2002. *Physical insight into the Ergun and Wen and Yu equations for fluid flow in packed and fluidised beds*. Chemical Engineering Science, 57(3): 527–534.

ParaView Home Page. Online: http://www.paraview.org/ (access: 1.05.2015).

Rainey T.J., Doherty W.O.S., Brown R.J., Kelson N.A., Martinez D.M. 2008. *Determination of the permeability parameters of bagasse pulp from two different sugar extraction methods*. TAPPI Engineering, Pulping & Environmental Conference. Portland, Oregon, United States, August 24–27.

Resch E. 2008. *Numerical and Experimental Characterisation of Convective Transport in Solid Oxide Fuel Cells*. MSc Thesis, Queens University, Kingston, Ontario, Canada.

Rossel S.M. 2004. *Fluid flow modeling of resin transfer molding for composite material wind turbine blade structures*. Sandia National Laboratories on-line report no SAND04-0076. Department of Chemical Engineering, Montana State University – Bozeman, Bozeman, Montana.

Samsuri A., Sim S.H., Tan C.H. 2003. *An Integrated Sand Control Method Evaluation*. Society of Petroleum Engineers, SPE Asia Pacific Oil and Gas Conference and Exhibition, Jakarta, Indonesia, 9–11 September.

Skjetne E., Klov T., Gudmundsson J.S. 1999. *High-Velocity Pressure Loss In Sandstone Fractures: Modeling And Experiments (SCA-9927)*. International Symposium of the Society of Core Analysts, Colorado School of Mines, Colorado, August 1–4.

Sobieski W. 2009a. *Calculating tortuosity in a porous bed consisting of spherical particles with known sizes and distribution in space*. Research report 1/2009, Winnipeg.

SOBIESKI W. 2009b. *Switch Function and Sphericity Coefficient in the Gidaspow Drag Model for Modeling Solid-Fluid Systems*. Drying Technology, 27(2): 267–280.

SOBIESKI W. 2010. *Examples of Using the Finite Volume Method for Modeling Fluid-Solid Systems*. Technical Sciences, 13: 256–265.

SOBIESKI W. 2014. *The quality of the base knowledge in a research process*. Scientific researches in the department of mechanics and machine design, University of Warmia and Mazury in Olsztyn, 2: 29–47.

SOBIESKI W., LIPINSKI S. *The PathFinder User's Guide*. Online: http://www.uwm.edu.pl/pathfinder/ (access: 1.05.2015).

SOBIESKI W., TRYKOZKO A. 2011. *Sensitivity aspects of Forchheimer's approximation*. Transport in Porous Media, 89(2): 155–164.

SOBIESKI W., TRYKOZKO A. 2014a. *Forchheimer Plot Method in Practice*. Part 1. *The experiment*. Technical Sciences, 17(4): 221–335.

SOBIESKI W., TRYKOZKO A. 2014b. *Forchheimer Plot Method in Practice*. Part 2. *A numerical model*. Technical Sciences, 17(4): 337–350.

SOBIESKI W., ZHANG Q., LIU C. 2012. *Predicting Tortuosity for Airflow Through Porous Beds Consisting of Randomly Packed Spherical Particles*. Transport in Porous Media, 93(3): 431–451.

The MayaVi Data Visualizer. Online: http://mayavi.sourceforge.net/index.html (access: 1.05.2015).

The PathFinder Project. Online: http://www.uwm.edu.pl/pathfinder/ (access: 1.05.2015).

WHITAKER S. 1996. *The Forchheimer equation: A theoretical development*. Transport in Porous Media, 25(1): 27–61.

WU J., YU B., YUN M. 2008. *A resistance model for flow through porous media*. Transport in Porous Media, 71(3): 331–343.

Guide for Autors

Introduction

Technical Sciences is a peer-reviewed research Journal published in English by the Publishing House of the University of Warmia and Mazury in Olsztyn (Poland). Journal is published continually since 1998. Until 2010 Journal was published as a yearbook, in 2011 and 2012 it was published semiyearly. From 2013, the Journal is published quarterly in the spring, summer, fall, and winter.

The Journal covers basic and applied researches in the field of engineering and the physical sciences that represent advances in understanding or modeling of the performance of technical and/or biological systems. The Journal covers most branches of engineering science including biosystems engineering, civil engineering, environmental engineering, food engineering, geodesy and cartography, information technology, mechanical engineering, materials science, production engineering etc.

Papers may report the results of experiments, theoretical analyses, design of machines and mechanization systems, processes or processing methods, new materials, new measurements methods or new ideas in information technology.

The submitted manuscripts should have clear science content in methodology, results and discussion. Appropriate scientific and statistically sound experimental designs must be included in methodology and statistics must be employed in analyzing data to discuss the impact of test variables. Moreover there should be clear evidence provided on how the given results advance the area of engineering science. Mere confirmation of existing published data is not acceptable. Manuscripts should present results of completed works.

There are three types of papers: a) research papers (full length articles); b) short communications; c) review papers.

The Journal is published in the printed and electronic version. The electronic version is published on the website ahead of printed version of Technical Sciences.

Technical Sciences does not charge submission or page fees.

Types of paper

The following articles are accepted for publication:

Reviews

Reviews should present a focused aspect on a topic of current interest in the area of biosystems engineering, civil engineering, environmental engineering, food engineering, geodesy and cartography, information technology, mechanical engineering, materials science, production engineering etc. They should include all major findings and bring together reports from a number of sources. These critical reviews should draw out comparisons and conflicts between work, and provide an overview of the 'state of the art'. They should give objective assessments of the topic by citing relevant published work, and not merely present the opinions of individual authors or summarize only work carried out by the authors or by those with whom the authors agree. Undue speculations should also be avoided. Reviews generally should not exceed 6,000 words.

Research Papers

Research Papers are reports of complete, scientifically sound, original research which contributes new knowledge to its field. Papers should not exceed 5,000 words, including figures and tables.

Short Communications

Short Communications are research papers constituting a concise description of a limited investigation. They should be completely documented, both by reference list, and description of the experimental procedures. Short Communications should not occupy more than 2,000 words, including figures and tables.

Letters to the Editor

Letters to the Editor should concern with issues raised by articles recently published in scientific journals or by recent developments in the engineering area.

Contact details for submission

The paper should be sent to the Editorial Office, as a Microsoft Word file, by e-mail: techsci@uwm.edu.pl

Referees

Author/authors should suggest, the names, addresses and e-mail addresses of at least three potential referees. The editor retains the sole right to decide whether or not the suggested reviewers are used.

Submission declaration

After final acceptance of the manuscript, the corresponding author should send to the Editorial Office the author's declaration. Submission of an article implies that the work has not been published previously (except in the form of an abstract or as part of a published lecture or academic thesis or as an electronic preprint), that it is not under consideration for publication elsewhere, that publication is approved by all authors and tacitly or explicitly by the responsible authorities where the work was carried out, and that, if accepted, it will not be published elsewhere in the same form, in English or in any other language.

To prevent cases of ghostwriting and guest authorship, the author/authors of manuscripts is/are obliged to: (i) disclose the input of each author to the text (specifying their affiliations and contributions, i.e. who is the author of the concept, assumptions, methods, protocol, etc. used during the preparation of the text); (ii) disclose information about the funding sources for the article, the contribution of research institutions, associations and other entities.

Language

Authors should prepare the full manuscript i.e. title, abstract and the main text in English (American or British usage is accepted). Polish version of the manuscript is not required.

The file type

Text should be prepared in a word processor and saved in doc or docx file (MS Office).

Article structure

Suggested structure of the manuscript is as follows:

Title
Authors and affiliations
Corresponding author
Abstract
Keywords
Introduction
Material and Methods
Results and Discussion
Conclusions

Acknowledgements (*optional*)
References
Tables
Figures

Subdivision – numbered sections

Text should be organized into clearly defined and numbered sections and subsections (optionally). Sections and subsections should be numbered as 1. 2. 3. then 1.1 1.2 1.3 (then 1.1.1, 1.1.2, ...). The abstract should not be included in numbering section. A brief heading may be given to any subsection. Each heading should appear on its own separate line. A single line should separate paragraphs. Indentation should be used in each paragraph.

Font guidelines are as follows:
– Title: 14 pt. Times New Roman, bold, centered, with caps
– Author names and affiliations:12 pt. Times New Roman, bold, centered, italic, two blank line above
– Abstract: 10 pt. Times New Roman, full justified, one and a half space. Abstract should begin with the word Abstract immediately following the title block with one blank line in between. The word Abstract: 10 pt. Times New Roman, centered, indentation should be used
– Section Headings: Not numbered, 12 pt. Times New Roman, bold, centered; one blank line above
– Section Sub-headings: Numbered, 12 pt. Times New Roman, bold, italic, centered; one blank line above
– Regular text: 12 pt. Times New Roman, one and a half space,full justified, indentation should be used in each paragraph

Title page information

The following information should be placed at the first page:

Title

Concise and informative. If possible, authors should not use abbreviations and formulae.

Authors and affiliations

Author/authors' names should be presented below the title. The authors' affiliation addresses (department or college; university or company; city, state and zip code, country) should be placed below the names. Authors with the same affiliation must be grouped together on the same line with affiliation information following in a single block. Authors should indicate all affiliations with a lower-case superscript letter immediately after the author's name and in front of the appropriate address.

Corresponding author

It should be clearly indicated who will handle correspondence at all stages of refereeing and publication, also post-publication process. The e-mail address should be provided (footer, first page). Contact details must be kept up to date by the corresponding author.

Abstract

The abstract should have up to 100-150 words in length. A concise abstract is required. The abstract should state briefly the aim of the research, the principal results and major conclusions. Abstract must be able to stand alone. Only abbreviations firmly established in the field may be eligible. Non-standard or uncommon abbreviations should be avoided, but if essential they must be defined at their first mention in the abstract itself.

Keywords

Immediately after the abstract, author/authors should provide a maximum of 6 keywords avoiding general, plural terms and multiple concepts (avoid, for example, 'and', 'of'). Author/authors should be sparing with abbreviations: only abbreviations firmly established in the field may be eligible.

Abbreviations

Author/authors should define abbreviations that are not standard in this field. Abbreviations must be defined at their first mention there. Author/authors should ensure consistency of abbreviations throughout the article.

Units

All units used in the paper should be consistent with the SI system of measurement. If other units are mentioned, author/authors should give their equivalent in SI.

Introduction

Literature sources should be appropriately selected and cited. A literature review should discuss published information in a particular subject area. Introduction should identify, describe and analyze related research that has already been done and summarize the state of art in the topic area. Author/authors should state clearly the objectives of the work and provide an adequate background.

Material and Methods

Author/authors should provide sufficient details to allow the work to be reproduced by other researchers. Methods already published should be indicated by a reference. A theory should extend, not repeat, the background to the article already dealt within the Introduction and lay the foundation for further work. Calculations should represent a practical development from a theoretical basis.

Results and Discussion

Results should be clear and concise. Discussion should explore the significance of the results of the work, not repeat them. A combined Results and Discussion section is often appropriate.

Conclusions

The main conclusions of the study may be presented in a Conclusions section, which may stand alone or form a subsection of a Results and Discussion section.

Acknowledgements

Author/authors should include acknowledgements in a separate section at the end of the manuscript before the references. Author/authors should not include them on the title page, as a footnote to the title or otherwise. Individuals who provided help during the research study should be listed in this section.

Artwork
General points

– Make sure you use uniform lettering and sizing of your original artwork
– Embed the used fonts if the application provides that option

– Aim to use the following fonts in your illustrations: Arial, Courier, Times New Roman, Symbol
– Number equations, tables and figures according to their sequence in the text
– Size the illustrations close to the desired dimensions of the printed version

Formats

If your electronic artwork is created in a Microsoft Office application (Word, PowerPoint, Excel) then please supply 'as is' in the native document format

Regardless of the application used other than Microsoft Office, when your electronic artwork is finalized, please 'Save as' or convert the images to one of the following formats (note the resolution requirements given below):

EPS (or PDF): Vector drawings, embed all used fonts

JPEG: Color or grayscale photographs (halftones), keep to a minimum of 300 dpi

JPEG: Bitmapped (pure black & white pixels) line drawings, keep to a minimum of 1000 dpi or combinations bitmapped line/half-tone (color or grayscale), keep to a minimum of 500 dpi

Please **do not**:
– Supply files that are optimized for screen use (e.g., GIF, BMP, PICT, WPG); these typically have a low number of pixels and limited set of colors
– Supply files that are too low in resolution
– Submit graphics that are disproportionately large for the content

Color artwork

Author/authors should make sure that artwork files are in an acceptable format (JPEG, EPS PDF, or MS Office files) and with the correct resolution. If, together with manuscript, author/authors submit color figures then Technical Sciences will ensure that these figures will appear in color on the web as well as in the printed version at no additional charge.

Tables, figures, and equations

Tables, figures, and equations/formulae should be identified and numbered consecutively in accordance with their appearance in the text.

Equations/mathematical and physical formulae should be presented in the main text, while tables and figures should be presented at the end of file (after References section). Mathematical and physical formulae should be presented in the MS Word formula editor.

All types of figures can be black/white or color. Author/authors should ensure that each figure is numbered and has a caption. A caption should be placed below the figure. Figure must be able to stand alone (explanation of all symbols and abbreviations used in figure is required). Units must be always included. It is noted that figure and table numbering should be independent.

Tables should be numbered consecutively in accordance with their appearance in the text. Table caption should be placed above the table. Footnotes to tables should be placed below the table body and indicated with superscript lowercase letters. Vertical rules should be avoided. Author/authors should ensure that the data presented in tables do not duplicate results described in figures, diagrams, schemes, etc. Table must be able to stand alone (explanation of all symbols and abbreviations used in table is required). Units must be always included. As above, figure and table numbering should be independent.

References

References: All publications cited in the text should be presented in a list of references following the text of the manuscript. The manuscript should be carefully checked to ensure that the spelling of authors' names and dates of publications are exactly the same in the text as in the reference list. Authors should ensure that each reference cited in the text is also present in the reference list (and vice versa).

Citations may be made directly (or parenthetically). All citations in the text should refer to:

1. Single author

The author's name (without initials, with caps, unless there is ambiguity) and the year of publication should appear in the text

2. Two authors

Both authors' names (without initials, with caps) and the year of publication should appear in the text

3. Three or more authors

First author's name followed by et al. and the year of publication should appear in the text

Groups of references should be listed first alphabetically, then chronologically.

Examples:

"... have been reported recently (ALLAN, 1996a, 1996b, 1999; ALLAN and JONES, 1995). KRAMER et al. (2000) have recently shown..."

The list of references should be arranged alphabetically by authors' names, then further sorted chronologically if necessary. More than once reference from the same author(s) in the same year must be identified by the letters "a", "b", "c" etc., placed after the year of publication.

References should be given in the following form:

KUMBHAR B.K., AGARVAL R.S., DAS K. 1981. *Thermal properties of fresh and frozen fish*. International Journal of Refrigeration, 4(3), 143–146.

MACHADO M.F., OLIVEIRA F.A.R., GEKAS V. 1997. *Modelling water uptake and soluble solids losses by puffed breakfast cereal immersed in water or milk*. In Proceedings of the Seventh International Congress on Engineering and Food, Brighton, UK.

NETER J., KUTNER M.H., NACHTSCHEIM C.J., WASSERMAN W. 1966. *Applied linear statistical models* (4th ed., pp. 1289–1293). Irwin, Chicago.

THOMSON F.M. 1984. *Storage of particulate solids*. In M. E. Fayed, L. Otten (Eds.), Handbook of Powder Science and Technology (pp. 365–463). Van Nostrand Reinhold, New York.

Citation of a reference as 'in press' implies that the item has been accepted for publication.

Note that the full names of Journals should appear in reference list.

Submission checklist

The following list will be useful during the final checking of an article prior to the submission. Before sending the manuscript to the Journal for review, author/authors should ensure that the following items are present:

– Text is prepared with a word processor and saved in DOC or DOCX file (MS Office). One author has been designated as the corresponding author with contact details: e-mail address

– Manuscript has been 'spell-checked' and 'grammar-checked'

– References are in the correct format for this Journal

– All references mentioned in the Reference list are cited in the text, and vice versa

– Author/authors does/do not supply files that are too low in resolution

– Author/authors does/do not submit graphics that are disproportionately large for the content